

1

2

3

4

5 **This version of the article has been accepted for publication in Pure and**
6 **Applied Geophysics, but is not the Version of Record and does not reflect**
7 **post-acceptance improvements, or any corrections.**

8

9

10

11

12 **Role of fluid on earthquake occurrence: Example of**
13 **the 2019 Ridgecrest and the 1997, 2009 and 2016**
14 **Central Apennines sequences**

15

16

Jugurtha Kariche^{1,2}

17

18

19

¹ USTHB, Laboratoire de Géophysique, FSTGAT, Algiers, Algeria.

20

² Institut Terre et Environnement de Strasbourg (ITES), CNRS-UMR7063.

21

22

23

24

*Corresponding author: Jugurtha Kariche (jugurtha.kariche@usthb.edu.dz or
25 jkariche@gmail.com)
26

26

27

28

29

30

31

32

33

34 **ABSTRACT**

35 This paper focuses on the study of the temporal evolution of seismicity and the role of fluids
36 during major earthquake sequences that occurred in the Central Apennines and Southern
37 Walker Lane belt-Eastern California Shear Zone over the last two decades: The 1997 Colfiorito,
38 the 2009 L'Aquila, the 2016 Amatrice-Norcia, and the 2019 Ridgecrest sequences. The
39 availability of high-quality earthquakes catalogs offers the opportunity to evaluate in detail the
40 temporal evolution of the earthquake's size distribution (or b-value) and propose a physical
41 explanation based on the effect of the fluid flow process in triggering seismicity. For all seismic
42 sequences, the b-value time series show a gradual decrease from a few months to one year
43 before mainshocks. The gradual decrease in the b-value is interpreted as a gradual increase in
44 earthquake activity due essentially to the short-term to intermediate-term pore-fluid
45 fluctuations. The temporal variation of the b-value during Amatrice-Norcia and Ridgecrest
46 foreshock sequences is characterized by a double b-value minimum separated by a short-lived
47 b-value increase as observed in laboratory experiments on water-saturated rocks. The observed
48 fluctuation of the b-value is presented here as an accelerating crack growth due essentially to
49 the fluid flow instability. Even though seismic precursors could have been predictable in areas
50 with high dense seismic networks, the different b-value time series reveal the difficulty in
51 establishing a correspondence between the duration of the foreshock activity and the magnitude
52 of the next largest expected earthquake. This may suggest that the fluid migration controls the
53 size of the ruptures.

54 **Key words:** Seismicity and tectonics; Fractures, faults, Fluids; Neotectonics

55

56

57

58 INTRODUCTION

59 Several studies have suggested a relation between the occurrence of earthquake sequences
60 and the temporal change in the relative size distribution of earthquakes quantified by the
61 Gutenberg-Richter (GR) b-value (Berg, 1968; Scholz, 1968; Smith, 1981; Wiemer & Wyss,
62 2000 among others). The analyses of a series of 60 foreshocks and 428 aftershocks related to
63 three moderate earthquakes occurring in the Fairbanks region of Alaska show that the
64 Gutenberg-Richter (GR) b-value was abnormally low (between 0.34 to 0.45) before large events
65 and was restored taking a typical value of 0.85 to 0.95 during and after each mainshock (Berg,
66 1968). The seismicity analysis of the 1967 Caracas (Mw 6.7) earthquake sequence, the 1971
67 San Fernando (Mw 6.4) earthquake sequence, and the 1968–1978 New Zealand earthquake
68 sequence reveals that the temporal variation in the b-value was remarkably coupled with the
69 size of moderate to strong earthquakes (Berg, 1968). A large time scale decrease in the b-value
70 associated with an acceleration of aseismic slip is observed before the Mw 8.1 Iquique, Chile,
71 and the Mw 9.0 Tohoku-Oki earthquakes (Nanjo et al., 2012; Scholz, 2019). Several studies
72 argue that the acceleration of aseismic slip is favored by variation of pore fluid pressure at depth
73 (Segall & Rice, 1995; Ruhl et al., 2016; Cappa et al., 2019 ; De Barros et al., 2020). The gradual
74 decrease in the b-value on a much shorter time scale is also observed in the four-month-long
75 foreshock sequence preceding the 2009 L'Aquila earthquake (Gulia et al., 2016). The temporal
76 variation of the b-value before the L'Aquila mainshock correlates with the change of V_p/V_s
77 from January to April 6 (Lucente et al., 2010). The simultaneous change in b-value and V_p/V_s
78 in the case of the L'Aquila sequence may be interpreted as a nucleation process due to an
79 overpressurized volume controlled by fluid migration at depth (Chiaraluce, 2012).

80 The comparison between the temporal evolution of b-value and the effective normal stress
81 in California shows a decrease in the b-value associated with a decrease in the effective normal
82 stress rate (Khoshmanesh & Shirzaei, 2018). The maximum increase in the Coulomb stress rate

83 (up to 0.45 bar/yr spanning the period from 2003 to 2010) along the central part of the San
84 Andreas Fault system also coincides with the decrease in effective normal stress caused by the
85 evolution of pore-fluid pressure at depth (Khoshmanesh & Shirzaei, 2018). These results argue
86 that a strong correlation exists between the fluid migration and the temporal evolution of the b-
87 value along the central part of the San Andreas Fault. In the Southern Walker Lane belt (SWL)–
88 Eastern California Shear Zone (ECSZ), high-resolution optical satellite imagery analysis
89 reveals a considerable contribution of the inelastic processes to the total diffuse deformation
90 following the 2019 Ridgecrest earthquake sequence (Antoine et al., 2021). The high V_p/V_s
91 ratio covering the complex fault zones of the 2019 Ridgecrest foreshock–mainshock sequence
92 (Tong et al., 2021) denotes that the change in the pore-fluid pressure near the Ridgecrest fault
93 zone may be considered as one of the plausible mechanisms explaining the diffuse inelastic
94 deformation observed during the 2019 Ridgecrest sequence. A stress change modeling result
95 taking into account the variation in the V_p/V_s ratio due to the diffusive effect of fluids during
96 the Mw 6.4 Ridgecrest foreshock indicates that the value of fluid diffusivity necessary to trigger
97 the next Mw 7.1 mainshock is estimated to be $\leq 2.32 \times 10^4 \text{ cm}^2/\text{s}$ (Kariche, 2022).

98 A laboratory fracturing experiment on fluid-saturated rocks predicts a variation in the
99 V_p/V_s due to the change in the rheological properties of the seismogenic crust following large
100 earthquakes. Fracture mechanics modeling and laboratory experiments for dry and water-
101 saturated specimens show that the gradual decrease in the b-value related to a progressive
102 increase in acoustic emission rate (AE) is only visible in water-saturated rocks (Main et al.,
103 1990). Laboratory experiments at constant pore-fluid volume also predict a fluctuation in the
104 b-value before major cracks and support the idea that the fluid considerably affects the size and
105 the distribution of future cracks (Sammonds et al., 1992). Other correlations between b-value
106 and fluid migration are also found in the crustal range of the Taiwan orogenic belt (Chen et al.,
107 2019). Although these studies have demonstrated a connection between the variation in the b-

108 value and the influence of fluids, none have successfully proposed a unified physical
109 mechanism that explains the occurrence of seismic sequences, the stress evolution, and the
110 effect of fluids across different phases related to the generation of earthquake sequences.

111 In this paper, I explore the influence of fluid migration on earthquake occurrence by analyzing
112 the temporal evolution of seismicity for two tectonically active zones with available high-
113 quality, dense seismic networks: the Central Apennines (Italy) and the SWL–ECSZ (CA).
114 Several major seismic sequences are studied in detail: the 1997 Colfiorito, the 2009 L’Aquila,
115 and the 2016 Amatrice–Norcia for the Central Apennines seismic zone, and the 2019 Ridgecrest
116 sequence for the SWL–ECSZ. These sequences are explored in terms of seismic productivity
117 and related fluid migration. By analyzing the evolution of seismicity and stress redistribution,
118 I found a causative relation between the pore-fluid effect and the spatiotemporal evolution of
119 crack growth before and during earthquakes. The results are also compared to the laboratory
120 experiments for a better constraint on the role of fluids in the different phases of earthquake
121 generation. Based on these findings, I propose a physical mechanism that connects pore-fluid
122 effects and stress redistribution in controlling the earthquake preparation process, including the
123 behavior of foreshock evolution. Using the poromechanical analysis as presented in this paper,
124 I further explore the influence of b-value changes on earthquake forecasting. Additionally,
125 considering poroelastic stress change modeling results and the analysis of postseismic
126 deformation processes, the influence of fluids on the occurrence of aftershock sequences is also
127 debated.

128 **SEISMOTECTONICS SETTING, FLUID FLOW AND MECHANICAL PROPERTIES** 129 **OF FAULT ZONES**

130

131 **1. THE CENTRAL APENNINE SEQUENCE**

132 The 1997, 2009, and 2016 Central Apennines earthquake sequences start with the 1997
133 Colfiorito (Umbria–Marche) sequence, which struck the northern part of the Apennines in Italy
134 (Amato *et al.*, 1998; Stramondo *et al.*, 1999; Deschamps *et al.*, 2000; Chiaraluce *et al.*, 2003).
135 The Colfiorito sequence is characterized by six earthquakes with a magnitude larger than 5.0
136 and two earthquakes with a magnitude larger than 5.7 (Figure 1, Figure 2A & S1). The first
137 earthquake occurred on September 26 at 00:33 UTC with a magnitude $M_w = 5.7$ (Ekström *et*
138 *al.*, 1998). Nine hours later, another strong earthquake with $M_w 6.0$ struck the Colfiorito region
139 at 3 km from the first event (Figure 1). The $M_w 5.7$ and $M_w 6.0$ events were preceded by a
140 series of foreshocks that began on September 3, occurring in the area between the epicenters of
141 the two main events (Ripepe *et al.*, 2000). The hypocentral depths of the $M_w 5.7$ and $M_w 6.0$
142 events are approximately equal and situated at 5.04 and 4.95 km depth, respectively (Figure
143 S1). The third event with a magnitude $M_w = 5.9$ triggers 18 days after at 12 km southeast of
144 the first event (Figure S1). The analysis of the spatial and temporal evolution of seismicity
145 related to the 1997 Colfiorito sequence shows that the seismicity is mainly controlled by the
146 poroelastic properties of the seismogenic zone and the fluid flow process (Antonioli *et al.* 2005).
147 Using the fluid triggering hypothesis, the value of fluid diffusivity associated with the triggering
148 process of the 1997 Colfiorito sequence is estimated to range between 2.2×10^5 and 9.0×10^5
149 cm^2/s (Antonioli *et al.*, 2005).

150 On April 6, 2009, at 01:32 GMT, a devastating earthquake with a magnitude $M_w 6.3$
151 occurred on a normal fault at the intramontane basin near the city of L'Aquila (Lucente *et al.*,
152 2010; Figure 1). This sequence began with a series of foreshocks six months prior to the
153 mainshock in a ~ 4 km long band on the L'Aquila fault zone (Figure 2B; Figures S3A and C).
154 The near-field seismic wave analysis shows that the spatiotemporal evolution of foreshocks
155 correlates with a clear variation in seismic wave properties at depth (Lucente *et al.*, 2010). The
156 V_p/V_s value rose from 1.85 to more than 1.92 near the epicenter area of the 2009 L'Aquila

157 earthquake a week before the mainshock, and decreased to 1.85 a few hours before (Lucente et
158 al., 2010). The change in V_p/V_s near L'Aquila is interpreted as the variation in elastic properties
159 of the medium due to the fluid migration along the L'Aquila fault zone (Lucente *et al.*, 2010;
160 Chiaraluce, 2012; Scholz, 2019). Based on the temporal change in the V_p/V_s ratio, the
161 triggering mechanism related to the L'Aquila earthquake is resolved as a mechanism governed
162 by the presence of a deep, large fluid reservoir (Lucente *et al.*, 2010). Indeed, the complexity
163 of the fault zone, the deep thrust fault, and the low-angle active normal faults observed near the
164 L'Aquila major rupture (Chiodini *et al.*, 2004) may be interpreted as a structural seal that favors
165 the fluid accumulation and creates an overpressurized volume near the L'Aquila hypocentral
166 depth.

167 From the structural point of view, the evolution of fault geometry near the L'Aquila fault
168 zone seems to be controlled by a set of conjugate EW–NS fault systems in a transtensional
169 regime at the limit of large active fault segments. The aftershock distribution analysis following
170 the 2009 L'Aquila mainshock indicates that a significant portion of the aftershock productivity
171 (~32% of the total aftershocks recorded during the period from April to December 2009) is
172 concentrated at the limit of the fault slip zone. Seismological investigations and pore-fluid
173 pressure modeling results suggest that the spatiotemporal evolution of aftershocks at the limit
174 of the L'Aquila fault was primarily driven by a reduction in fault strength of 7–10 MPa, largely
175 attributed to the fluid-flow processes (Malagnini *et al.*, 2012).

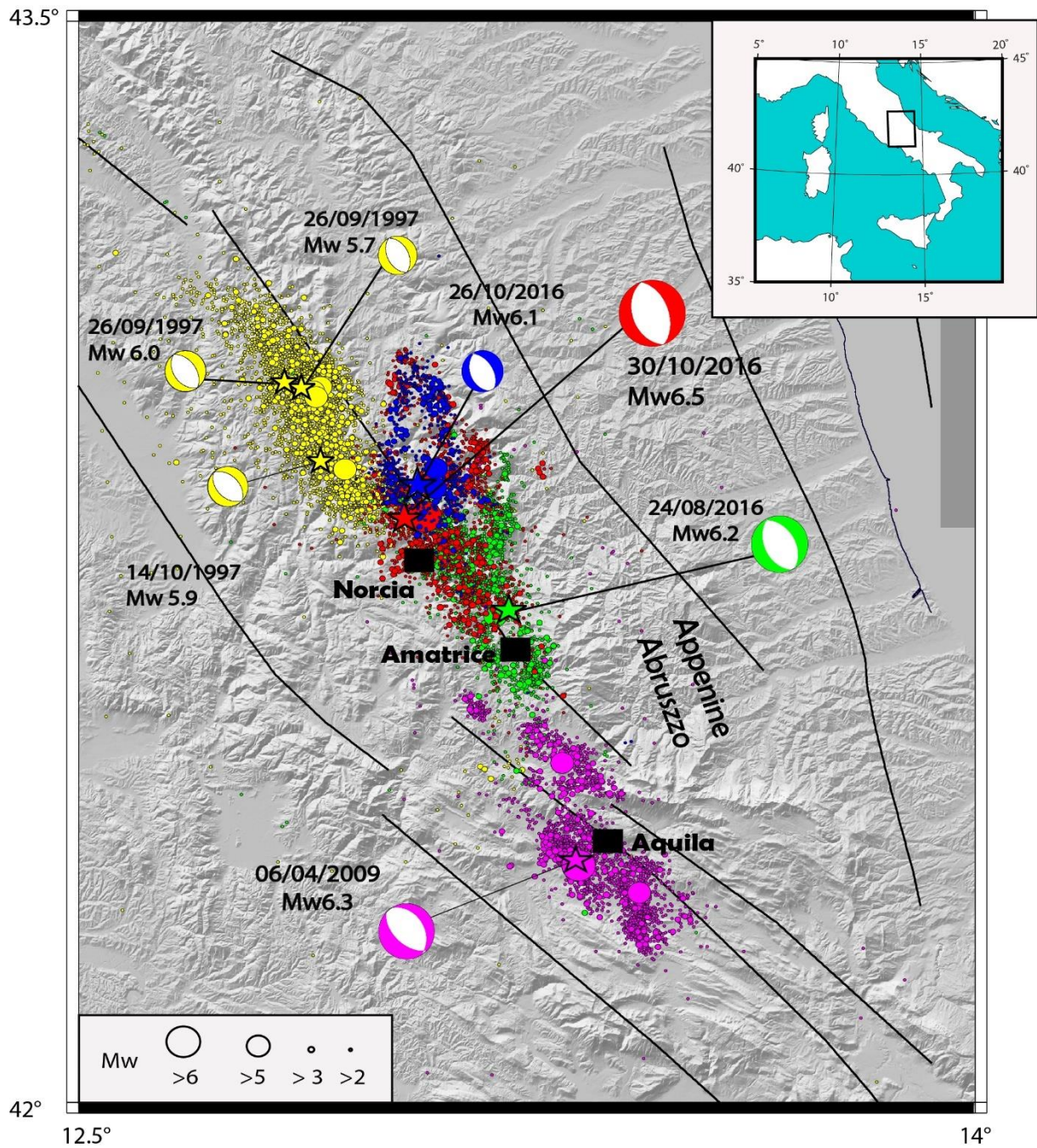
176 After the 2009 L'Aquila earthquake, the Central Apennine was followed by three moderate
177 earthquakes with a magnitude $M \geq 6.0$: the 2016 August 24 Amatrice earthquake (M_w 6.2), the
178 2016 August 26 Ussita (Visso) earthquake (M_w 6.1), and the 2016 October 30 Norcia
179 earthquake (M_w 6.5) (Figure 1). Thus, this sequence fills the gap between the Colfiorito and
180 L'Aquila earthquake series (Figure 1). The focal mechanism of the three earthquakes shows a
181 normal faulting solution (Figure 1) consistent with the active extension rate of 3–4 mm/yr in

182 the Apennines zones revealed by GPS (Serpelloni *et al.*, 2005). The mechanics of deformation
183 in the Central Apennines are complex. The strain release near the Amatrice fault zone is
184 accommodated by a complex interaction between the main normal faults and secondary
185 structures inherited from the pre-Quaternary compressional tectonic phases (Cheloni *et*
186 *al.*,2017).

187 The spatiotemporal analysis of seismicity between the Amatrice and Visso earthquakes predicts
188 a fluid diffusivity value of 1.5 m²/s, corresponding to a northward migration rate of 0.4 km/day
189 (Pino *et al.*, 2019; Tung & Masterlark, 2018). However, the fluid diffusivity along individual
190 fault branches within the 2016 Amatrice–Norcia earthquake sequence reveals a range of fluid
191 diffusivity between 50 and 2000 m²/s (Malagnini *et al.*, 2022). The differences in fluid
192 characteristics reported by various authors (Antonioli *et al.*, 2005; Tung & Masterlack, 2018;
193 Pino *et al.* 2019; Malagnini *et al.*, 2022) correlate with the variation in seismicity from south to
194 north in the Apennine fault zone (Figure 1). This variation in fluid diffusivity may explain the
195 high degree of heterogeneity along the Apennines fault zone and the differences in the time
196 characteristics between major earthquakes.

197

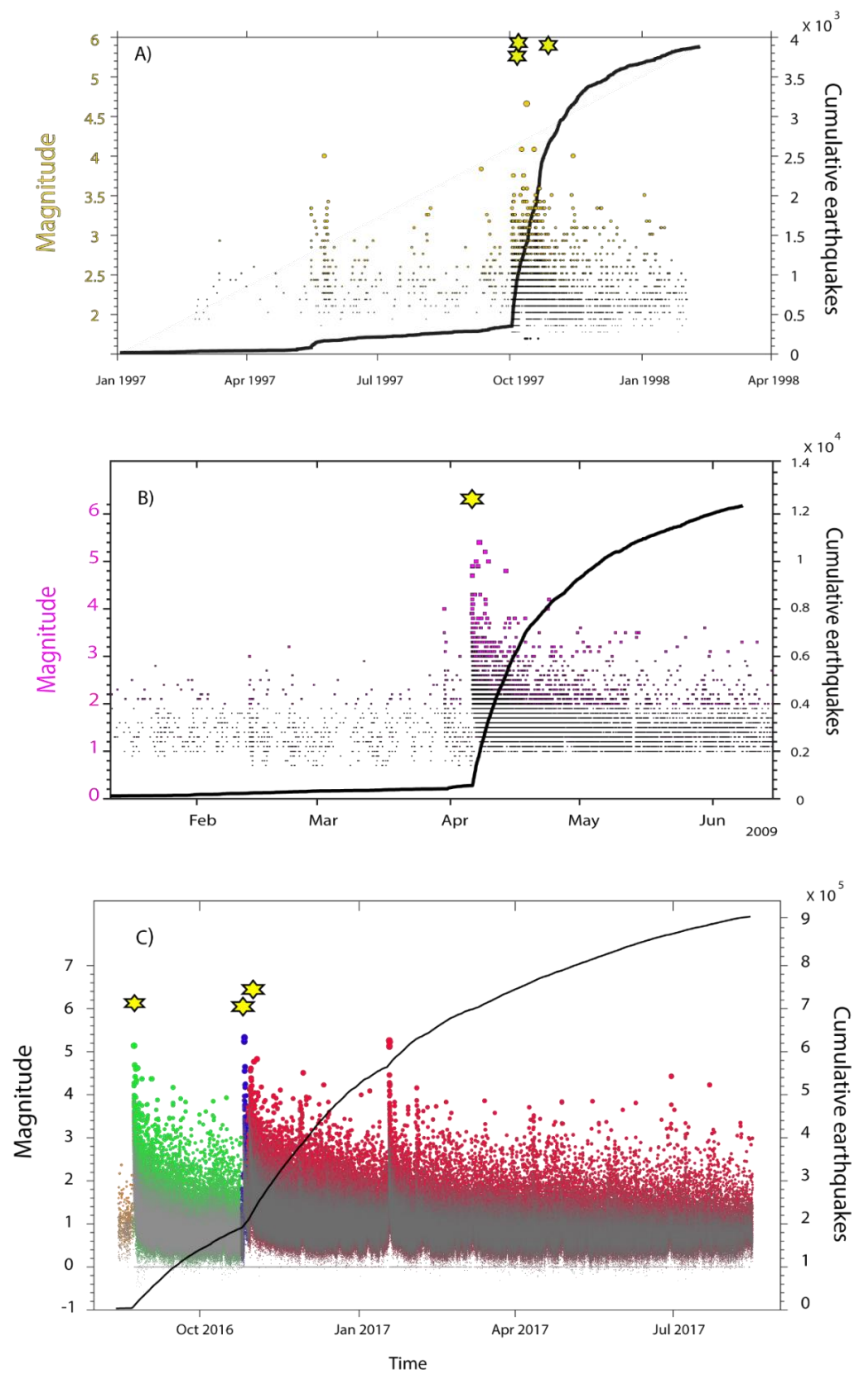
198



199

200 **Figure 1:** Seismicity and focal mechanisms of major earthquakes occurred in the central
 201 Apennines (Italy) spanning the period from 1997 to 2016. Each earthquake sequence with a
 202 related mainshock focal mechanism is represented by specified color. For example, the
 203 magenta color represents the spatial distribution of the events associated with the 2009
 204 L'Aquila earthquake sequence, the focal mechanism associated to the L'Aquila mainshock is
 205 also represented by the same color. The focal solutions are from the Global Centroid Moment

206 *Tensor* (<https://www.globalcmt.org/>). The seismicity of the Central Apennine is from INGV
 207 (<https://doi.org/10.13127/ISIDE>). The inset figure represents the location of the studied area.
 208 Note that the 2016 Amatrice-Norcia seismic sequence may view as a unique earthquake swarm
 209 divided into three smaller sequences. The colored data (green, blue, red) mimic the seismic
 210 migration from the August 24th (sequence in green), and culminating with the October 30th, Mw
 211 6.5 earthquake (sequence in red).



213 **Figure 2:** *Evolution of the Cumulative number of earthquakes and magnitude distribution*
214 *through time for: A) the 1997 Colfiorito sequence, B) the 2009 L'Aquila sequence and C) the*
215 *2016 Amatrice-Norcia sequence. The earthquakes datasets used for A) and B) are from INGV*
216 *(<https://doi.org/10.13127/ISIDE>). The earthquake database used for construct the C) plot is*
217 *derived from a high precise determination of ~900, 000 earthquakes derived from deep-neural-*
218 *network-based picker (Tan et al., 2021). The earthquake magnitude evolution in time from each*
219 *sequence is represented by a specific color same as in Figure 1. The yellow stars represent the*
220 *major events for each sequence. The Time evolution of earthquakes and related magnitude*
221 *distribution are constructed using the Zmap software (Wyss & Wiemer., 2000).*

222 **2. THE 2019 RIDGECREST SEQUENCE**

223 In July 2019, two moderate to strong earthquakes with a magnitude Mw 6.4 and 7.1 struck
224 Ridgecrest (California) in the SWL–ECSZ region (Fielding *et al.*, 2020). Earthquake rupture
225 characteristics deduced from Interferometric Synthetic Aperture Radar (InSAR), source time
226 functions, and early aftershock analysis indicate that the Mw 6.4 and the Mw 7.1 earthquakes
227 occurred on strike-slip faults within a time interval approximately equal to 34 hours at 12 km
228 distance and ranging depth of 4 to 8 km (Figure 3; Barnhart *et al.*, 2019; Fielding *et al.*, 2020,
229 Toda & Stein, 2020). Early surface deformation analysis deduced from InSAR and focal
230 mechanism analysis indicate that the 2019-07-04 (Mw 6.4) and the 2019-07-06 (Mw 7.1) events
231 occurred on NE–SW and NW–SE trending conjugate strike-slip faults. The Ridgecrest fault
232 zone is a part of the Indian Wells Valley, which is connected to the Central Basin and Range
233 tectonic province. This area is bounded on the west by the Sierra Nevada Mountains, on the
234 south by the Garlock fault, and on the east by the Walker Lane belt (Figure 3). The Little Lake
235 (or Ridgecrest) fault zone (LLFZ) is defined as an important component of the SWL–ECSZ
236 which accommodates a non-negligible part of the Pacific–North America plate boundary
237 displacement (Figure 3). The seismotectonics of the Ridgecrest region reflect the complex

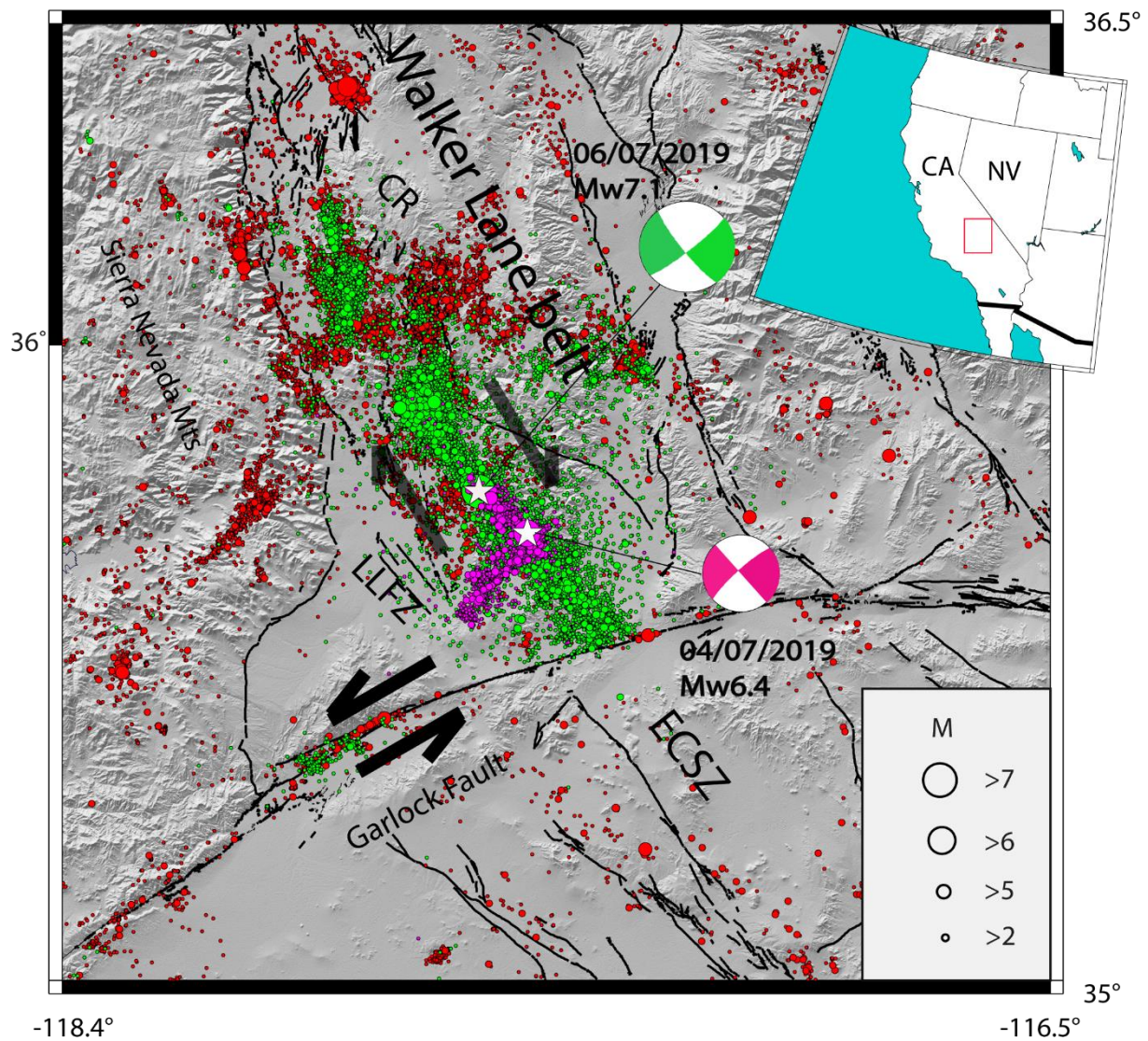
238 interaction of left-lateral and right-lateral strike-slip faults in a variable tectonic regime (Figure
239 3). The transition from transpressional regimes near LLFZ to transtensional regimes north of
240 Ridgecrest (near Coso Range) agrees with the rotation of the maximum principal stress (Combs
241 1980). This may be interpreted as a consequence of a significant weakening mechanism
242 affecting immature faults. In this context, pressurized fluids trapped within heterogeneous and
243 complex fault zones experience dynamic changes in fluid flow processes. These changes tend
244 to reduce effective normal stress and, consequently, influence the strength of the faults during
245 the early stages of fault-rupture growth.

246 Based on the poromechanical model proposed by Rice (1992), Axen (1992) interprets the
247 active deformation along the low-angle normal fault in the Indian Wells Valley–Coso Range as
248 a consequence of a weakening mechanism due to abnormally elevated pore-fluid pressure in
249 both brittle and ductile regimes. In this case, the permeability in the active fault zone must be
250 higher than its surrounding rocks. Large volumes of fluid migrating from ductile to brittle zone
251 in active mylonite areas are also observed in relation to the detachment zones in the Central
252 Mojave Desert (Axen, 1992). The analysis of high-resolution imaging derived from satellite
253 optical imagery shows that the presence of inelastic failure related to the 2019 Ridgecrest
254 earthquake sequence reflects a mylonitic deformation of the fault damage zone (Barnhart *et al.*,
255 2020). The observed mylonitic zones are directly correlated to the degree of fault maturity of
256 the Ridgecrest conjugated ruptures. The analysis of Line-of-Sight (LOS) Interferometric
257 Synthetic Aperture Radar (SAR) displacements following the 2019 Ridgecrest sequence attests
258 that a part of the observed early 2019 Ridgecrest postseismic deformation is indicative of a
259 poroelastic rebound (Wang & Bürgmann, 2020). The LOS displacements derived from both
260 Sentinel-1 and COSMO-SkyMed (CSK) SAR data reveal that the maximum postseismic
261 deformation along the LOS of ascending satellite tracks is located northwest of the Mw 7.1
262 epicenter near the Coso geothermal fault zone (Wang & Bürgmann, 2020).

263 Most of the seismicity recorded before the 2019 Ridgecrest sequence is relatively small (M
264 ≤ 3). The largest event recorded in SWL is the 1872 $M7.5$ Owens Valley earthquake (Figure
265 S2; Monastero *et al.*, 2002). The 1872 $M7.5$ Owens Valley earthquake is dominated by a right-
266 lateral shearing deformation along the Owens Valley fault (Figure S2). The recurrence of
267 earthquakes with a magnitude $M \geq 5.0$ in SWL is approximately equal to 20 years, with two
268 significant sequences with four moderate events ($M \geq 5.0$) that occurred near Ridgecrest
269 between 1995 and 1998 (Hauksson *et al.*, 1995). This recurrence pattern has culminated in the
270 occurrence of the 2019 Ridgecrest sequence (M_w 6.4; M_w 7.1). The study of the mechanics of
271 earthquake and fault interaction in the context of conjugate strike-slip faults indicates a clear
272 influence of fluid migration on the occurrence of moderate to large earthquakes in the SWL
273 tectonic domain (Kariche, 2022). Based on the Coulomb poroelastic stress change modeling
274 approach, the time delay between two conjugate strike-slip earthquakes seems to be coupled to
275 the variation in fluid diffusivity along heterogeneous faults (Kariche, 2022). These observations
276 are in concordance with the Cocco & Rice (2002) Coulomb stress transfer modeling results
277 taking into account the presence of high pore-fluid pressure at hypocentral depth.

278 Considering the ~ 34 hr characteristic time representing the time delay between the M_w 6.4
279 and the M_w 7.1 events (Kariche, 2022) and a fluid viscosity of 3×10^{-4} Pa·s, the average value
280 of permeability necessary to trigger the M_w 7.1 Ridgecrest event is estimated between 10^{-14} –
281 10^{-15} m². Despite the fact that this value is higher than the value obtained by Cocco and Rice
282 (2002) for normal fault geometries, it seems to be in good agreement with the permeability
283 values obtained by Miller (2020) for the 1992 Landers–Big Bear conjugated sequence and
284 based entirely on the conceptual model of permeability dynamics as proposed by the same
285 author. Additionally, this estimation of permeability aligns well with the value obtained by
286 Nespoli *et al.* (2018) for the 2012 Emilia–Romagna earthquake sequence. The temporal and
287 spatial evolution of major events following the M_w 6.4 foreshock sequence may explain the

288 significant increase in the value of permeability along cracks following the Mw 7.1 event. Based
 289 on this assumption, the temporal distribution of earthquake frequency and related moment
 290 release must predict a temporal fluctuation of the G–R b-value during the 2019 Ridgecrest
 291 sequence caused essentially by the variation of pore-fluid pressure at depth.



292 -118.4° -116.5° 35°

293 **Figure 3:** Seismicity along the Southern Walker Lane (SWL)-Eastern California Shear zone
 294 (ECSZ) from 2008 to 27/10/2019 using combined SCEDC QTM catalog (Ross et al. 2019) and
 295 the high definition NEIC-USGS catalog. The color circles indicate the seismicity at different
 296 periods: red from the period between 1980 and July 2019; magenta for the period covering
 297 the 2019 Ridgecrest foreshock activity and green for events following the Mw7.1 mainshock.

298 *The stars show the location of the (Mw 6.4) and the 06/07/2019 (Mw 7.1) earthquakes. The red*
299 *rectangle in the inset figure represents the studied area. LLFZ= Little Lake Fault Zone. CR=*
300 *Coso Range. CA=California State. NV= Nevada State.*

301 **METHODOLOGY AND DATA**

302 It's widely recognized that elevated fluid pressure exerts a crucial role in earthquake-
303 triggering mechanics by reducing the frictional strength of the fault (Hickman *et al.*, 1995;
304 Sibson, 2000; Yamashita & Tsutsumi, 2018a; Kariche *et al.*, 2018). The fluid-flow process can
305 also play a fundamental role during earthquake sequences by encouraging the production of
306 aftershocks (Nur & Booker, 1972; Malagnini *et al.*, 2012; Kariche *et al.*, 2018; Chiarabba *et*
307 *al.*, 2020). To quantify the influence of fluids in the nucleation, growth, and development of
308 large-scale earthquakes and related aftershock sequences, I use several techniques based on
309 both earthquake statistics and physics. The first step consists of developing a conceptual model
310 based on the joint analysis of the temporal evolution of the earthquake frequency–magnitude
311 distribution and pore-fluid flow before and during the Ridgecrest and Central Apennines
312 sequences. The analysis is also constrained by poroelastic stress change modeling scenarios and
313 previous laboratory results on fractured rocks (e.g., Sammonds *et al.*, 1992) in order to give a
314 robust estimation of the role of fluids on earthquake generation. The second step is to investigate
315 a physics-based model of aftershock occurrence on the basis of the assumption that the
316 production of aftershocks is intimately linked to the fluid-flow diffusion process. As for the
317 first step, the analysis of the influence of the fluids on aftershock generation is also aided by
318 poroelastic stress change modeling results taking into account both undrained and drained fluid
319 phases.

320 **1. G-R b-value time series modeling**

321 A first empirical relation between the frequencies and magnitudes of earthquakes is proposed
322 by Gutenberg & Richter (1950):

$$323 \quad \text{Log}_{10}[N(M)] = a - bM \quad (1)$$

324 Where a and b are the G-R constants, M is the magnitude, and $N(M)$ is the number of
325 earthquakes in a specific time window of events with a magnitude range between M and $\pm \delta M$.

326 The b-value for an entire catalog is given by the maximum likelihood estimation (Aki, 1965):

$$327 \quad b = \frac{1}{\ln(10)(\bar{M} - M_c)} \quad (2)$$

328 Where \bar{M} represents an average magnitude value for a population of earthquakes satisfying the
329 condition $M \geq M_c$, and M_c is the magnitude of completeness defined as the lowest magnitude
330 at which all the events in a space-time volume are detected (Wiemer & Wyss, 2000; Woessner
331 & Wiemer, 2005).

332 The b-value time series can be rewritten as (Woessner & Wiemer, 2005):

$$333 \quad b = \frac{\text{Log}_{10}(e)}{[\langle M \rangle - (M_c - \Delta M_{bin}/2)]} \quad (3)$$

334 Where $\langle M \rangle$ represents the mean magnitude of the sample and ΔM_{bin} is the binning width of the
335 catalogue (Aki, 1965).

336 The standard deviation of b-value can be obtained using the Shi & Bolt (1982) approach:

$$337 \quad \delta b = 2.3 b^2 \sqrt{\frac{\sum_i (M_i \{M\})}{n(n-1)}}$$

338 Where n is the sample size. The term $\sum_i (M_i \{M\})$ is related to the distribution function of the
339 mean magnitude where $\{M\}$ define the mean magnitude.

340 **Earthquake Data and Completeness**

341 In order to evaluate the temporal variation of seismicity on a seismogenic volume, the
342 variation in b-value is computed using the 3D frequency–magnitude approach (Wyss *et al.*,
343 1998) with an appropriate time window. The procedure adopted here consists of varying the
344 time-length windows to provide a robust estimation of the b-value at each point in time. The b-
345 value time series computation procedure used in this study is, in general, similar to those used
346 by Gulia & Wiemer (2019) or Dascher-Cousineau *et al.* (2020), which take into account the
347 space–time evolution of M_c in the b-value estimation. The determination of M_c is based on the
348 assumption that the seismic events are self-similar (Wiemer & Wyss, 2000). The most robust
349 way to deal with the dependence of the b-value time series on M_c is to choose a large value of
350 M_c for the entire time series catalog, but this approach leads to maximizing uncertainties when
351 the computation of the b-value is made for a smaller number of earthquake samples.

352 The completeness magnitude (M_c) for each earthquake sample is assessed using an
353 automated procedure that accounts for its temporal variability, based on the Maximum
354 Curvature (MAXC) method (Wiemer & Wyss, 2000), M_c and the corresponding b-value are
355 estimated simultaneously by identifying the maximum of the first derivative of the frequency–
356 magnitude distribution. In regions with dense seismic networks and access to high-quality
357 catalogs, the MAXC technique enables a reliable time-resolved estimation of b-values. It also
358 reduces uncertainties associated with smaller sample sizes, which often affect fixed- M_c
359 approaches. The latter may obscure short-term b-value variations due to over-smoothing.

360 To mitigate the known underestimation of M_c by the MAXC method, a correction factor
361 of +0.2 to +0.5 is systematically added (Table 1). This adjustment accounts for the observation
362 that the overall shape of the b-value time series remains robust across a range of reasonable M_c
363 values specific to each earthquake sequence.

364 For periods with limited instrumental coverage, particularly in the Italian earthquake
365 catalog between 1998 and 2005, when M_c may remain elevated over extended intervals, a fixed
366 M_c approach is preferred (Table 1). This method reduces bias in b-value estimation and avoids
367 artificial inflation of b-values caused by unrecognized drops in M_c due to undetected small-
368 magnitude events. By applying a uniform magnitude threshold across all time windows,
369 including those affected by seismic gaps, the fixed M_c approach ensures greater consistency
370 than MAXC in this context. This, in turn, enhances the interpretability of b-value temporal
371 trends, as M_c becomes decoupled from fluctuations in catalog completeness. Conversely, for
372 events occurring after 16 April 2005, when higher-resolution data are available, the MAXC
373 method is preferred.

| Earthquake Sequence | Time Period | Mc Values | Methodology / Notes |
|-----------------------------|---------------------------|------------|---|
| 2019 Ridgecrest | Before Mw 6.4 | 0.84 – 1.4 | Estimated using MAXC method, corrected by +0.2 – 0.5 for stability |
| | Between Mw 6.4 and Mw 7.1 | 0.66 – 1.2 | Final consistent $M_c \approx 1.4$ used for robust time series. Temporal b-value estimates remain stable within $M_c \in [1.1, 2.0]$ via Lilliefors test |
| | After Mw 7.1 | 0.4 – 1.2 | |
| 2016 Amatrice-Norcia | Full Seq | 0.9– 2.3 | Estimated using MAXC method, corrected by +0.2 – 0.5 for stability, results validated via bootstrapping Temporal b-value estimates remain stable within $M_c \in [2.1, 2.5]$ via Lilliefors test |
| 2009 L'Aquila | Foreshock Seq | 1.4 | MAXC method with a correction factor of +0.2 aligned with Gulia et al. (2016) predictive approach MAXC method consistent with a Fixed M_c |
| 1997 Colfiorito | Full Seq | 2.5 | Fixed M_c with $\delta M_c = 0.1-0.2$; used for stable estimates; comparable with variable- M_c result trends. |

374 Table1: Summary of M_c values and technics used in b-value time series computation.

375 For the 2019 Ridgecrest sequence, I use the high-confidence Quake Template Matching
376 (QTM) seismicity catalog for Southern California (Ross *et al.*, 2019), which spans the period
377 from 2000 to 2018, along with the USGS-NEIC updated high-resolution catalog from March
378 2018 to March 2020, and the higher-resolution dataset from Shelly (2020) focused on the
379 Ridgecrest aftershock sequence. For the 1997, 2009, and 2016 Central Apennines sequences, I
380 rely on the complete seismic catalog of the Istituto Nazionale di Geofisica e Vulcanologia
381 (INGV), covering the period from 1985 to 2018 (<https://doi.org/10.13127/ISIDE>), in
382 combination with the regional catalog by Gasperini *et al.* (2013), augmented by the high-
383 resolution catalog from Tan *et al.* (2021) for the 2016–2017 Amatrice–Norcia sequence.
384 Duplicate events resulting from the combination of multiple catalogs are automatically
385 identified and removed using the ZMAP software (Wiemer, 2001). A space–time window
386 algorithm (e.g. Gardner & Knopoff, 1974) is applied to flag similar events occurring within
387 defined proximity in both space and time. The catalogs are then merged into a single file, with
388 redundant events eliminated accordingly. For more details on magnitude homogenization and
389 catalog processing, refer to the “EARTHQUAKE MAGNITUDE” section in the
390 Supplementary Material.

391 To investigate in detail the role of fluids before and after major earthquakes, I compare the
392 temporal evolution of the b-value in the Central Apennines with that observed following the
393 2019 Ridgecrest sequence (Table 1). The b-value time series method involves analyzing the
394 frequency–magnitude distribution over sliding time windows of fixed event counts. This
395 approach allows more accurate estimation of b-value changes over time, improving our ability
396 to constrain seismicity evolution across periods of highly variable seismic rates (Tormann *et al.*, 2013). Assuming that the b-value time series reflects the temporal evolution of crack density
397 or stress heterogeneity in a seismogenic zone, the M_c threshold for each time window is selected
398 in accordance with the magnitude distribution. b-values are computed using the maximum

400 likelihood method (Wyss & Wiemer, 2000), and temporal variations in M_c are incorporated in
401 the analysis following each mainshock to minimize the influence of completeness bias on the
402 resulting b-value time series.

403 The Ridgecrest zone is divided into $0.15^\circ \times 0.15^\circ$ grids. The computation is made regarding
404 the approach based on a fixed number of events of 250 with a 50 minimum event higher than
405 the local value of M_c by using the MAXC method with magnitude binning equal to 0.1.
406 Considering the change in the M_c value, I obtain an M_c value range of [0.84, 1.4] before the
407 Mw 6.4 event and [0.66, 1.2] from the period between the Mw6.4 and Mw7.1 Ridgecrest
408 mainshocks. After the Mw7.1 event, the M_c value range between [0.4, 1.2] (see Table 1). In
409 order to reduce uncertainties on the b-values estimations, and as mentioned before, I assess M_c
410 using the maximum curvature approach and I add 0.2-0.5 to the value of M_c . I confirm that the
411 value of M_c that gives a reasonable estimate of the temporal evolution of the b-value is about
412 1.4 (Figures S5, S7; S8). Furthermore, using the Lilliefors test for statistical validation, I
413 confirm that b-value estimates remain stable within a completeness magnitude range of **[1.1,**
414 **2.0]** (Table 1; see also the “ANALYSIS AND ROBUSTNESS OF THE B-VALUE AND M_c ”
415 section in the Supplementary Material). A similar methodology was applied to the Central
416 Apennines earthquake sequences (Table 1). In these cases, the MAXC technique also produced
417 reliable time-resolved b-value estimates while reducing uncertainty due to small sample sizes,
418 especially when compared to other estimation methods (Figures S4, S6, S9, S10).

419 Multiple b-value time series tests were performed using varying event counts, ranging from
420 50 to 500 events per window (Figures S11, S12). These variations allowed for an effective
421 balance between signal resolution and smoothing. The earthquake occurrence time was used to
422 define the temporal windows, which yielded a sampling interval of approximately 1 to 12
423 months, depending on the window size. Importantly, the overall shape of the b-value time series
424 remained stable for $100 \leq N \leq 500$ in both the 2016 Amatrice–Norcia and 2019 Ridgecrest

425 sequences (Figures S11, S12). These findings are consistent with earlier studies, such as Wyss
426 & McNutt, (1998) in their analysis of the 1989 earthquake swarm beneath Mammoth Mountain
427 (CA) and Tormann *et al* (2013) who modeled temporal correlations between b-value changes
428 and surface creep in the Parkfield (California) region.

429 **2. Fluid flow and the evolution of seismicity**

430 Taking into account the complexity of earthquake generation, a realistic representation of
431 the temporal evolution of seismicity following a seismic event can be expressed as (Utsu 1969;
432 Utsu & Ogata 1995):

$$433 \quad \frac{dN(t)}{dt} \propto \frac{k}{(c + t)^p} \quad (4)$$

434 Where $\frac{dN(t)}{dt}$ represents the aftershock frequency, t is the time from the mainshock-triggered
435 event, k is the productivity of aftershocks that depends on the total number of events, p is the
436 power-law exponent, and c defines the time delay before the onset of the power-law aftershock
437 decay rate and depends on the rate of activity in the earlier part of the seismic sequence. The
438 value of c is also related to the incompleteness of seismic catalogs after strong earthquakes.
439 Guo & Ogata (1997) obtained a range of c values between 0.003–0.3 days for various
440 earthquake datasets. In our simulation, the c value is fixed at 0.01 d. The value of c is selected
441 to be the lowest possible to obtain sufficient aftershock productivity in the very early part of
442 the aftershock sequence (Enescu *et al.*, 2007; Kariche *et al.*, 2018).

443 Based on the Nur and Booker (1972) hypothesis, the aftershock frequency rate within a
444 seismogenic volume can be proportional to the temporal evolution of pore-fluid pressure as :

$$445 \quad \frac{dN}{dt} = \frac{1}{\alpha} \int \frac{\partial P}{\partial t} dv \quad (5)$$

446 Where α is a constant that relate the rate of aftershock occurrence to the fluid pressure change
447 $\frac{\partial P}{\partial t}$ integrated over a given volume v . In a 2-D fluid flow model, as developed by Nur & Booker
448 (1972), the appropriate volume v defines the integration volume as the lower half-space. In our
449 context, the term "appropriate volume" refers to the area where slip produces significant
450 dilatation. P represents the pore-fluid pressure variation following an earthquake.

451 The model proposed here supposes that the high pore-fluid pressures are mainly
452 concentrated in an area with low permeability that has the potential to maintain elevated pore
453 pressure over time. For the Central Apennines and Ridgecrest aftershock sequences, the basic
454 idea is that a transient pore pressure is created along a fault zone by the dilatancy–fluid diffusion
455 mechanism. The slip phase leads to reduced fluid pressure along the fault plane, which is later
456 restored during the drained fluid phase in response to the redistribution of fluid along the
457 dilatant fault. The fault zone may act as a barrier and conduit of fluid simultaneously if we
458 suppose an anisotropy of permeability. Regarding the structural aspect, fluid migration may
459 take place through adjacent subsidiary fractures connected to bounding faults that are directly
460 associated with earthquake and aftershock behavior (Kirkpatrick *et al.*, 2008; Kariche *et al.*,
461 2018). Additionally, the arrangement of subsidiary fractures, their petrophysical properties, and
462 other topological characteristics may create localized deformed zones that serve as barriers and
463 fluid traps, leading to an accumulation of pore-fluid pressure (Yehya *et al.*, 2018).

464 The elevated pore-fluid pressure affects the effective normal stress and creates a zone of
465 unstable sliding that controls the aftershocks' productivity. The thermal pressurization effect
466 caused by the mainshock may also be viewed as a mechanism that generates elevated pore-fluid
467 pressure over time. However, experiments conducted in freshly fractured rocks suggest that
468 thermal pressurization might not offset the pore pressure changes caused by the dilatancy
469 process (Brantut, 2020). This finding is further supported by theoretical studies on both mature
470 and immature faults, which indicate that slip-induced dilatancy tends to dominate over thermal

471 pressurization effects (refer to Yamashita & Tsutsumi, 2018; Section 5.6). Consequently, it is
 472 plausible to consider the issue within a "steady-state" scenario, where the diffusion of pore fluid
 473 may act as a rate-controlling mechanism for the aftershock sequence.

474 Taking into account the boundary conditions for a steady-state source and assuming a one-
 475 dimensional Darcy flow, a simple poroelastic solution is given by Malagnini *et al.* (2012):

$$476 \quad P(x, t) = (P_0 - P_1) \operatorname{erfc} \left(\frac{x}{2\sqrt{ct}} \right) + P_1 \quad (6)$$

477 Where c represents the value of fluid diffusivity and erfc is the complementary error function.
 478 For nucleation assisted by fluids, Abramowitz & Stegun (1970) wrote the erfc function as:

$$479 \quad \operatorname{erfc} \left(\frac{x}{2\sqrt{ct}} \right) = \frac{2}{\sqrt{\pi}} \int_{\frac{x}{2\sqrt{ct}}}^{\infty} e^{-\xi^2} d\xi \quad (7)$$

480 In this case, the initial and boundary conditions may be posed as:

$$481 \quad \begin{cases} P(x = 0, t > 0) = P_0 = \lambda_f \rho_r g z \\ P(x > 0, t = 0) = P_1 = \rho_w g z \end{cases}$$

482 Where ρ_r and ρ_w are respectively the rocks and fluid density, λ_f is the pore fluid pressure
 483 coefficient for an arbitrary depth and range between 0.6 and 0.8 for fault reactivation assisted
 484 by fluid (Rikitake 1972). Z represents the source depth and g the gravitational acceleration.

485 Replacing the 1D pore-fluid pressure form in the Nur & Booker (1972) equation with the
 486 complementary error function, a complete aftershock pore-fluid diffusion solution may be
 487 written as:

$$488 \quad \frac{dN}{dt} = \frac{1}{\alpha} \frac{(P_0 - P_1)}{2\sqrt{\pi ct^3}} \int_0^{\infty} x e^{\left(-\frac{x^2}{4ct}\right)} dx = \frac{(P_0 - P_1)\sqrt{c}}{\alpha\sqrt{\pi}} \frac{1}{\sqrt{t}} \quad (8)$$

489 This equation shows that in the presence of high pore-fluid pressure, the aftershock decay rate
 490 is proportional $\frac{1}{\sqrt{t}}$. However, if an external source does not provide a sufficient fluid volume,
 491 the change in pore pressure becomes non-stationary as time t elapses.

492 Considering the problem as non-steady, the pore pressure decays rapidly and would be one-half
 493 of that associated with intermediate time scales. As a result, the decay in pore-fluid pressure is
 494 counterbalanced by the redistribution of shear stress along the fault caused essentially by the
 495 elastic fault's compaction (Biot, 1965; Booker, 1974; Brantut, 2020). Taking into account the
 496 coupling between the pore pressure and the elastic stress (i.e., Coulomb's law), the productivity
 497 of aftershocks over a large time scale can only occur if the time variation of shear stress exceeds
 498 the time variation in shear strength along faults. Assuming an elemental length of fault rupture,
 499 the aftershocks' decay rate may be seen as an integral of the time derivative of shear stress as:

$$500 \quad \frac{dN}{dt} = \int_{-1}^1 \frac{\partial}{\partial t} \tau_{xz}(x, t) dx \quad (9)$$

501 If we consider the hypothesis that aftershock production is essentially driven by stress load due
 502 to the fault compaction, the stress state along small-scale ruptures may be expressed as (Booker,
 503 1974):

$$504 \quad \tau_{xz}(x, t) = \frac{-H(t)}{\pi(1-x^2)} [1 - \beta F(x, t)] \quad (10)$$

505 where: $H(t)$ represents the Heaviside step function, β is the value of compressibility during the
 506 relaxation process, where the fluid is assumed to play no role, and $F(t, x)$ is an analytic function
 507 defined as (Booker, 1974):

$$508 \quad F(x, t) = 2t \left\{ \frac{1+x}{(1-x)^2} [1 - e^{-(1+x)^2/4t}] + \frac{1-x}{(1+x)^2} [1 - e^{-(1+x)^2/4t}] \right\} \quad (11)$$

509 Based on Equations 9, 10, and 11, the long-term decay of aftershock frequency, associated with
 510 the stress redistribution along fractured rocks, can be described by Booker's approximation as
 511 follows:

$$512 \quad \frac{dN}{dt} = \frac{1}{4}(1 - e^{-4/t}) + \lim_{\xi \rightarrow 0} \frac{1}{\xi^2} [1 - e^{-\xi^2/t}] \approx \frac{1}{t} \quad (12)$$

513 This solution indicates that, for a sufficient duration of time, the aftershock frequency decay
 514 resulting from the pore-pressure drop and the redistribution of shear stress along fractures
 515 would replicate the Omori-type signal.

516 **3. Modeling Fault Interactions and Fluid Effects**

517 To compute a static stress change caused by major earthquakes on nearby fault ruptures,
 518 I use the concept of Coulomb stress change on a fixed receiver fault. The applied stress change,
 519 calculated as the Coulomb Failure Function (ΔCFF ; e.g. Reasenberg & Simpson, 1992), is
 520 expressed by:

$$521 \quad \Delta CFF = \Delta\tau - \mu (\Delta\sigma_n - \Delta P) \quad (13)$$

522
 523 Where τ is the shear stress, σ_n is the normal stress (compression positive), P is the pore-fluid
 524 pressure, μ' is the coefficient of internal friction, and Δ refers to changes during the earthquake.
 525 The second term in Equation (13), defining the Terzaghi effective normal stress, may be
 526 replaced by the notion of effective friction coefficient as:

$$527 \quad \Delta CFF = \Delta\tau - \mu' \Delta\sigma_n \quad (14)$$

528
 529
 530 The apparent (or effective) friction μ' is given by Reasenberg & Simpson (1992) as follows:

$$531 \quad \mu' = \mu (1 - B) \quad (15)$$

532
 533
 534 where μ is the friction coefficient and B is the Skempton coefficient, which defines the
 535 relationship between the stress change and pore pressure change (Rice & Cleary, 1976; Beeler
 536 et al., 2000).

537

538 At the intermediate between undrained and drained fluid phases, the Skempton coefficient

539 B may be related to the undrained and drained state of fluids as (Yamashita & Tsutsumi, 2018):

540
$$\frac{K}{K_u} = 1 - \alpha B$$

541 Where α is called the Biot & Willis coefficient (Biot, 1965) and represents the ratio

542 between the increment of fluid content and the volumetric strain change following an

543 earthquake. K and K_u represent the drained and undrained bulk moduli, respectively, and may

544 be written as a contribution of undrained (v_u) and drained (v) Poisson ratios (Yamashita &

545 Tsutsumi, 2018a):

546
$$\frac{K}{K_u} = \left(\frac{1 + v}{1 + v_u} \right) \times \frac{v_u}{v}$$

547 If an isotropic poroelastic model is assumed (Beeler et al., 2000), an intermediate short-term

548 poroelastic solution can be obtained by combining shear, normal, and pore-fluid contributions

549 as:

550
$$\Delta CFF = \Delta\tau - \mu \left(\Delta\sigma_n - \frac{(v_u - v)}{\alpha(1 - 2v)(1 + v_u)} \Delta\sigma_{kk} \right) \quad (16)$$

551 Equation (16) demonstrates that the influence of pore fluids is not maximized during the

552 undrained phase but becomes significant as the system transitions toward the drained phase.

553 This behavior has been previously investigated by Segall and Rice (1995) and Chambon and

554 Rudnicki (2001), who explored stress changes resulting from fault geometries using a spring-

555 slider model applied to dilating, fluid-saturated faults.

556 In cases where rocks are fully saturated and exhibit a high density of pre-existing fractures

557 (v_u, v) = 0.31, 0.15 (Rice & Cleary, 1976; Bosl & Nur, 2002), the average poroelastic stress

558 response on target faults is approximately 40% greater than the Coulomb stress modeled using

559 only the elastic properties of the upper crust. Based on this fact, the presence of fluids along the

560 fault zone results in a short-term coupled poroelastic response that enhances stress loading on
561 fixed receiver faults. This occurs particularly in regions where fluid diffusion increases pore-
562 fluid pressure over time.

563 However, the absence of a fully realized 3D poroelastic model limits the ability to
564 physically characterize the complex and complete processes of fluid diffusion along active
565 faults. To address this, the cumulative stress change associated with the full poroelastic
566 relaxation following an earthquake is modeled using analytical 3D poroelastic solutions derived
567 from 3D elastic modeling. This approach incorporates the temporal variation of the Poisson
568 ratio as fluids transition from an undrained to a fully drained state (Segall, 2010, Sect. 10.7).
569 Rather than being an oversimplification, this methodology compares elastic deformation
570 scenarios between the "undrained" fluid state (immediately after the earthquake) and the fully
571 "drained" state (when fluid redistribution and heterogeneous fluid pressure equilibrium are
572 established along the fault zone). While it does not explicitly explore the detailed temporal
573 evolution of fluid migration and crustal deformation, the variation of the Poisson ratio from the
574 undrained to drained states is interpreted as a consequence of changes in rock rheology driven
575 by fluid drainage along the fault zone.

576 **RESULTS AND ANALYS**

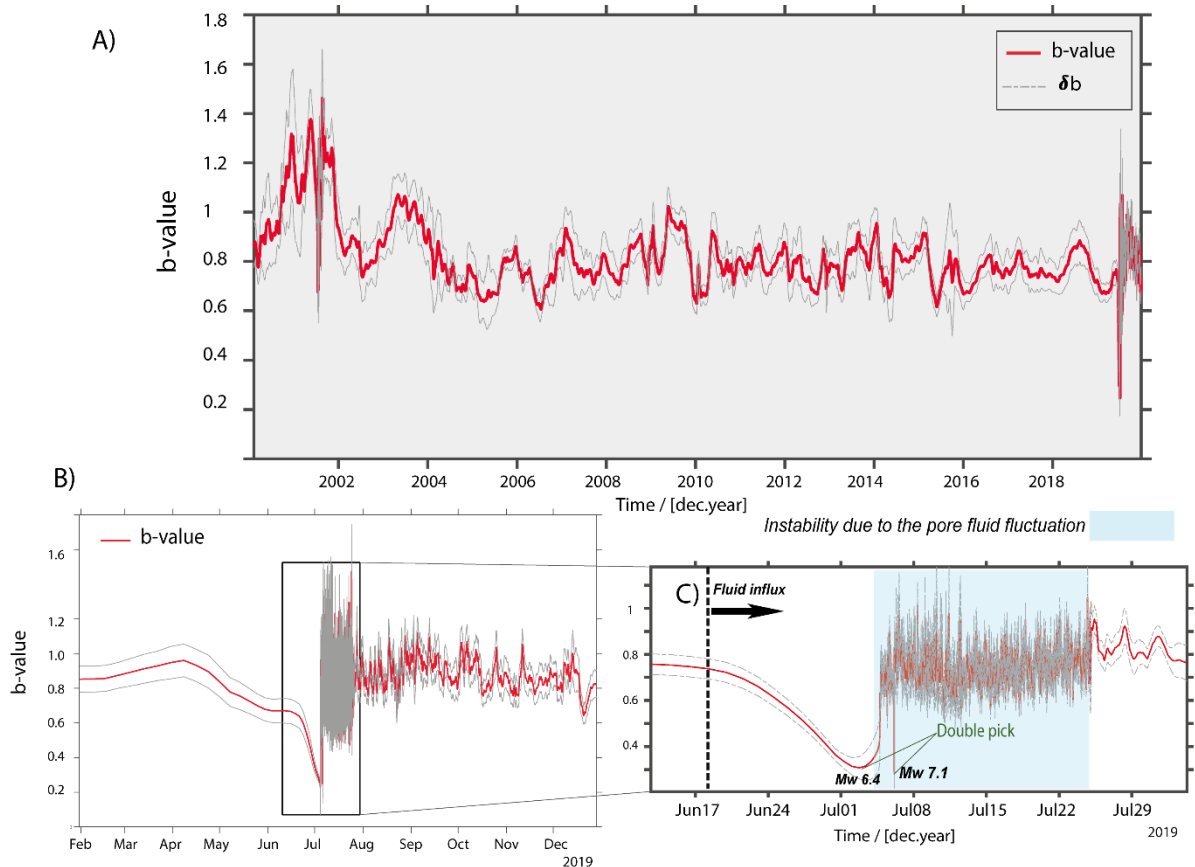
577 **1. TEMPORAL VARIATION OF B VALUE, FORESHOCK ANALYSIS AND THE** 578 **ROLE OF FLUID**

579 Figure 4 shows the preferred b-value time series for the Ridgecrest case. The optimum time
580 series calculation is made with a sample size of 250 events at a low window overlap (~4%).
581 The temporal evolution of the earthquake size distribution shows an increase in b-value one
582 year before the 2019 Ridgecrest sequence followed by a gradual decrease in b-value ~ one
583 month before the Mw 6.4 foreshock (Figures 4; 5 and S7A). After the Mw 6.4 earthquake, the

584 b-value rapidly varies from minimum to maximum and from maximum to minimum just before
585 the Mw7.1 earthquake showing major double peaks (Figures 4C and 5A) as predicted by the
586 laboratory experiments in water-saturated specimens (e.g., Main et al., 1989). The recovery in
587 b-value before the Mw 7.1 earthquake as observed in Figures 4 and 6A is interpreted here as a
588 response to pore pressure drop during the undrained phase of the fluid. This value is close to
589 the value of $b \sim 1$ during the left-lateral earthquake but the increase in foreshocks productivity
590 caused by fluid migration and pore pressure instability in the ~ 33 hours preceding the Mw7.1
591 right-lateral earthquake tends to re-decrease the b-value to ~ 0.5 creating a double b-value
592 minimum as observed in Figures 4C, 5A, 5C, and 6A.

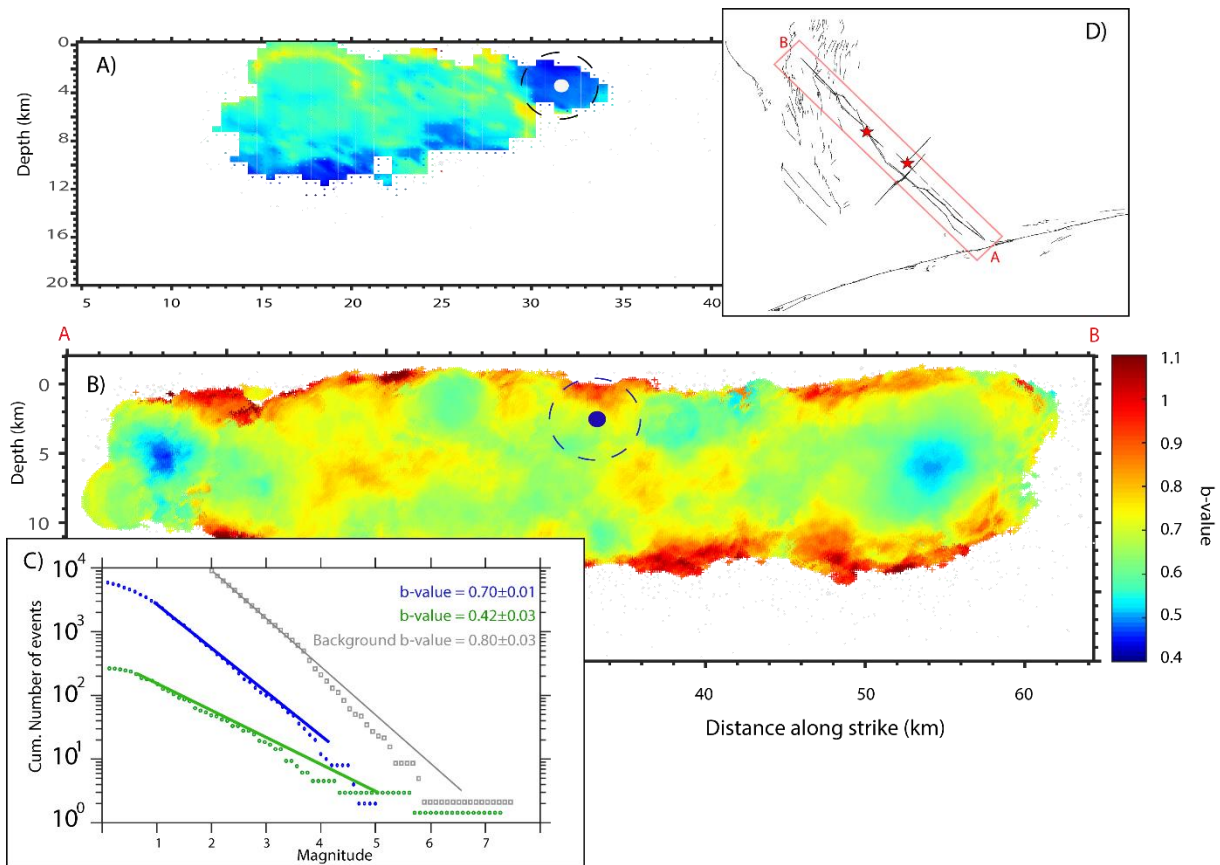
593 The Mw 7.1 shear rupture is accomplished by evolving the ensemble of foreshock events
594 off the Mw6.4 main rupture. This may be represented by a highly oriented diffusive seismicity
595 that grows in a shear zone of intense deformation. Therefore, the Mw7.1 dynamic failure does
596 not occur at peak stress (Figure S13A) and the failure process seems to be more dependent on
597 the temporal evolution of seismicity and related pore-fluid pressure redistribution nearby the
598 Mw7.1 nucleation area (Figure S13C) rather than the variation in elastic stress. In this case, the
599 minimum doublet b-value as observed in the b-value time series may be interpreted as a local
600 dilatancy hardening phase resulting from fluid migration along conjugate fault ruptures. At this
601 time, the fluid migration at a short time scale requires a significant evolution of the permeability
602 along fault ruptures. Based on this assumption and other considerations in relation to the stress
603 change induced by fault geometries in a spring-slider model for dilating fluid-infiltrated fault
604 (Segall & Rice, 1995; Chambon & Rudnicki, 2001), the temporal fluctuation of the b-value
605 related to the 2019 Ridgecrest sequence seems to be controlled by slip instability due essentially
606 to the pore pressure fluctuation caused by fluid migration along the heterogeneous fault zone.
607 The temporal b-value instability associated with the pore pressure fluctuation continues during
608 the two months following the Mw7.1 earthquake (Figures 4B and C). The \sim two-month

609 instability period may also represent the duration of the Mw 7.1 poroelastic rebound. Also, the
 610 similarities between the temporal evolution of the b-value for the 2019 Ridgecrest and the 2016
 611 Amatrice-Norcia sequences (Figures 6A, 6B and S13) may suggest an analogous physical
 612 mechanism controlling the foreshock occurrence for both sequences.



613

614 **Figure 4:** Earthquake size distribution estimates for the Ridgecrest fault zone area. **A)** b-value
 615 time series spanning the period from 2000 to 2020. The b-value time series were computed using the
 616 maximum curvature approach for a moving window of 250 events with a step size of 50 events. The
 617 window overlap is fixed at $\sim 4\%$. The Standard deviation of the b-value (δb) is represented by a dashed
 618 grey line and is obtained using the maximum likelihood estimation approach (Shi & Bolt 1982). **B)**
 619 Zoom-in figure for the period from February 2019 to January 2020. **C)** Zoom-in figure for the period
 620 from ~ 2 weeks before the 2019 Mw 6.4 first earthquake to August 01, 2020, but by adding a high
 621 smoothing plot factor (~ 6) to the b-value estimations.



622

623 **Figure 5:** *Spatio-temporal evolution of the b-value associated with the 2019 Ridgecrest sequence: A)*
 624 *cross-section showing b-value distribution before the Mw7.1 earthquake. B) Cross-section showing a*
 625 *b-value distribution after the Mw7.1 earthquake. C) Frequency-Magnitude Distributions (FMD)*
 626 *around the Mw7.1 hypocentral area before and after the Mw7.1 event: the green curve represents the*
 627 *G-R distribution before the Mw7.1 event, the blue curve represents the G-R distribution after the*
 628 *Mw7.1 and the gray curve represents the background FMD distribution. The dashed colored circles in*
 629 *A) and B) represent the locations of events used in C). D) Position of the cross-section with respect to*
 630 *the surface distribution of the Ridgecrest fault ruptures. The Ridgecrest Fault-ruptures are from Xu et*
 631 *al., (2020). The Quaternary faults are from the USGS.*

632 The double b-value minima as observed in Figure 6B correlates with the relative crustal
 633 velocity fluctuation observed in Amatrice-Norcia seismogenic zone (Soldati *et al.*, 2019). Note
 634 that the difference between Figure 4C and 6A in the 2-3 weeks preceding the Mw 6.4 earthquake
 635 is attributed to the use of a higher smoothing factor. The smoother curve in Figure 4C is
 636 employed solely to distinguish between the high and low-frequency b-value time series, thus

637 providing more accurate estimates of the temporal instability associated with the pore fluid
638 fluctuations. It is noteworthy that the b-value time series with a double b-value minimum
639 shown in Figure 4 is consistent with the b-value estimates obtained taking into account the Mc
640 values obtained by the Lilliefors test (Table 1; also refer to the “ANALYSIS AND
641 ROBUSTNESS OF THE B-VALUE AND MC” section in the Supplementary Material).
642 Additionally, the b-value mapping in Figure 5 aligns with the estimates derived from the EMR
643 technique proposed by Nanjo (2020) for the same sequence, particularly during the period
644 preceding the Mw 7.1 event. The key difference is that Nanjo (2020) exclusively uses a static
645 elastic stress change modeling procedure to explain the observed low b-value near the Mw 7.1
646 nucleation zone.

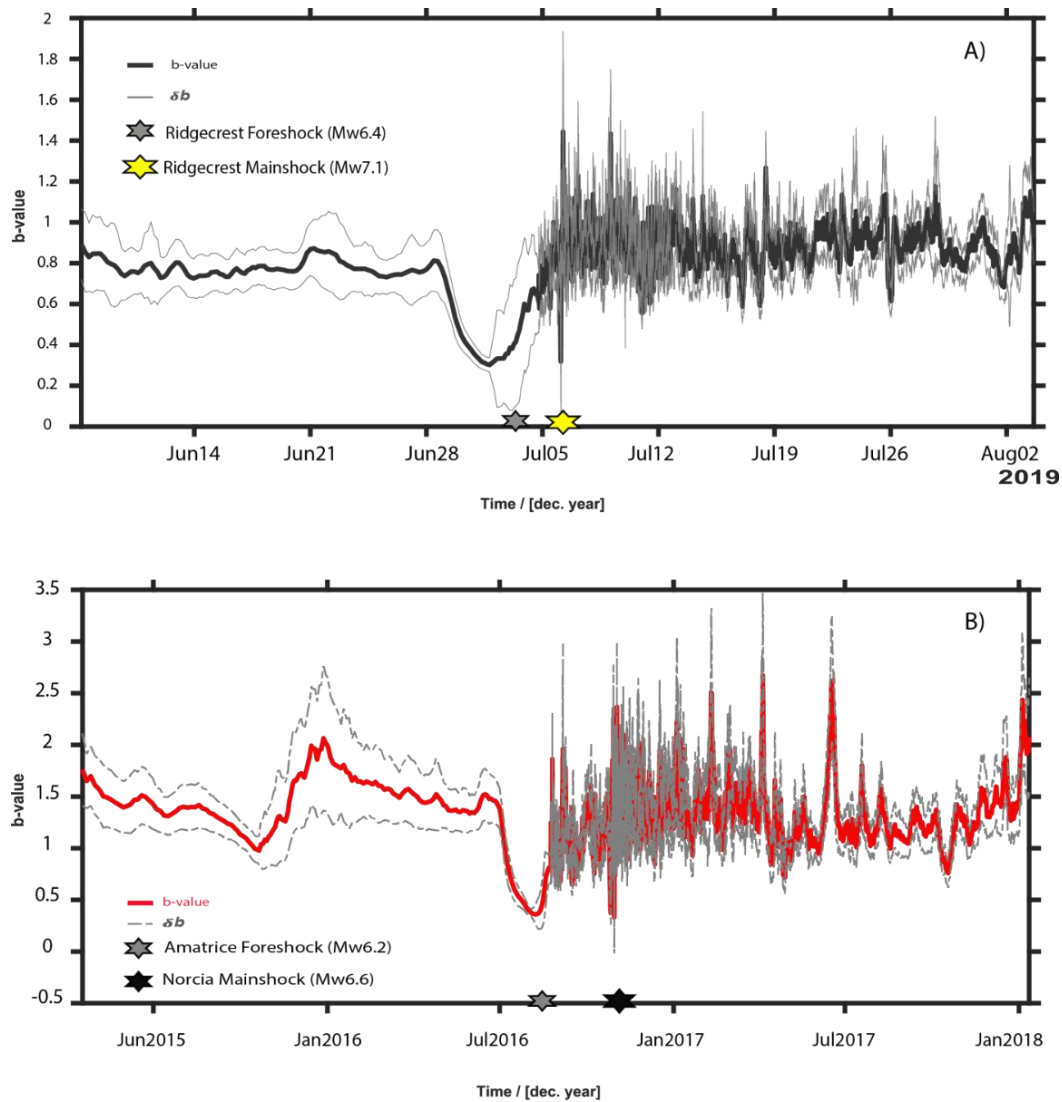
647 Considering the case of the 1997 Colfiorito sequence, the gradual decrease in the b-value
648 prior to the foreshock sequence (Figures 7C and 7D) seems to be concordant with the fracture
649 model of Main *et al.* (1990). Adopting the Main *et al.* (1990) experimental model of cracks, the
650 temporal evolution of the b-value may be defined here as a rapid failure after periods of strain
651 hardening and strain softening due essentially to the pore-fluid diffusion process. The dilatancy
652 softening phase related to the 1997 Colfiorito sequence seems to be controlled by the fluid
653 migration along fault zones where the stress intensity is highly coupled to the temporal variation
654 in effective normal stress. Considering the Terzaghi Law, the fluid diffusion phase will play a
655 crucial role in accelerating seismicity by decreasing the magnitude of effective normal stress
656 acting along cracks, promoting the occurrence of fast slip episodes at short time scale.

657 The time evolution of the b-value following the 2009 L’Aquila sequence differs from those
658 obtained for the 2016 –Amatrice-Norcia and the 2019 Ridgecrest sequences (Figures 6 and 8).
659 This difference may be due to the presence of a large deep fluid reservoir near the L’Aquila
660 fault zone which maintains a high pore fluid pressure during a large period of time. In fact,
661 InSAR time series analysis related to the central Apennine earthquakes reveals that the

662 sedimentary basin nearby the L'Aquila fault zone had experienced about 10 mm of accelerating
663 subsidence in the years prior to the L'Aquila mainshock (Moro *et al.* 2017) in agreement with
664 the observed change in the frequency of the b-value time series (Figure 8).

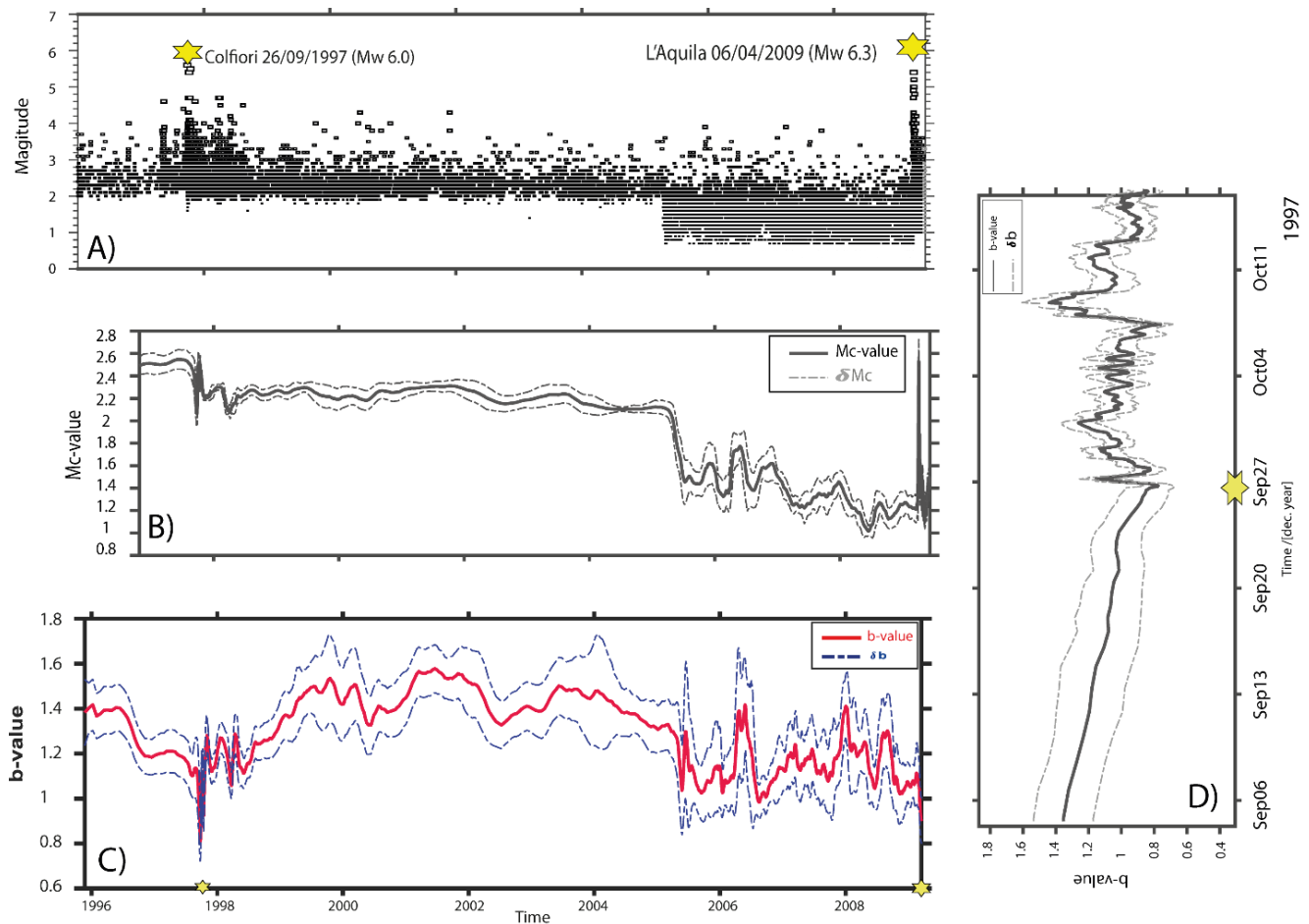
665 The accelerating subsidence is viewed as a consequence of large pre-earthquake fluid
666 migration along the fault zone (Moro *et al.* 2017). Based on our estimation of the b-value
667 (Figures 7 and 8) and ground deformation estimated from SAR imagery (Moro *et al.*, 2017),
668 the acceleration of subsidence is interpreted here as probably due to large dilatancy-fluid
669 diffusion processes that control the temporal fluctuations of the b-value at a large time scale.
670 The analysis of the time-magnitude series shows a gradual decrease in the number of events
671 with magnitude $M < 3$ associated with an increase of events with magnitude > 3.5 in agreement
672 with the change in the b-value time series (Figures 7 A and 8). A second phase with an apparent
673 increase of small magnitude earthquakes accompanied by a decrease in the number of events
674 with a magnitude M_w larger than 3.5 is observed in the two months prior to the 2009 L'Aquila
675 mainshock (Figures 7 A and 8). The gradual increase of micro-seismic events observed in the
676 two months prior to the L'Aquila mainshock is highly coupled with the gradual decrease in the
677 b-value (Figure 8; Figures S3A and B).

678 The trend of the b-value time series during the last phase of the L'Aquila interseismic
679 period is understood here as an influx of pore fluid into a dilatant volume near the nucleation
680 zone. The increase in the magnitude of foreshocks just before the L'Aquila mainshock (Figure
681 8) considerably affects the temporal evolution of the b-value by creating a sudden drop in the
682 b-value. The time delay between the start of foreshocks and the b-value decrease seems to
683 correlate with the gradual increase in microseismic events followed by a sudden increase in
684 earthquakes with magnitude $M \geq 3.0$ (Figure 8). This temporal-spatial clustering of seismicity
685 may suggest a complex stress evolution, consistent with a heterogeneous effective stress drop
686 modulated by fluid migration within a structurally anisotropic fault zone.



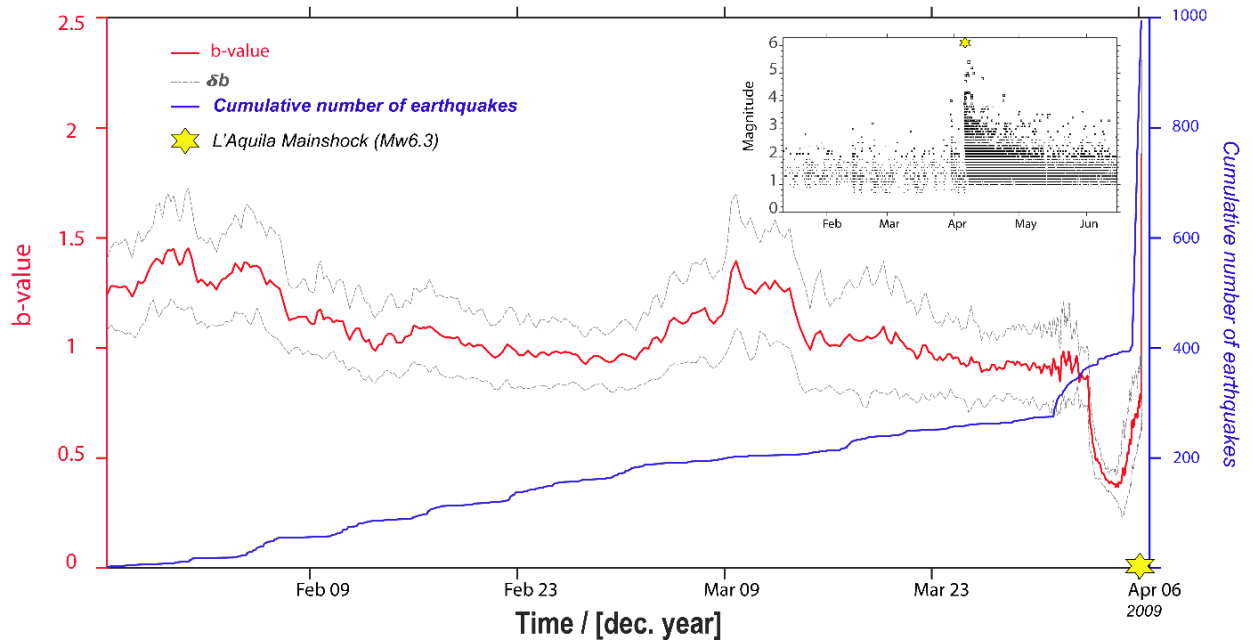
687

688 **Figure 6:** Comparison between *b*-value time series analysis following: **A)** 2019 Ridgecrest sequence
 689 and **B)** 2016 Amatrice-Norcia sequence. The two figures show a double pick during the foreshock –
 690 mainshock period as predicted by the laboratory experiments on water saturated specimens. The *b*-
 691 value time series is performed using the combined high resolution NEIC-USGS catalogs and
 692 supplemented by the Shelly (2020) catalog for events that occurred during the 2019 Ridgecrest
 693 foreshock-mainshock sequence. The *b*-value time series for the 2016 Amatrice-Norcia sequence is
 694 performed using the entire catalog of the INGV combined with the local catalogs published by Tan et
 695 al. (2021). The *b*-values time series are computed using ZMAP7.0. For both sequences, the uncertainty
 696 estimation is obtained by 100 bootstraps related to windows size of 250 events.



697

698 **Figure 7. A)** Earthquake magnitude versus time for the central Appennines covering the periods
 699 between 1996 to 2009 and using combined catalogs of INGV and Gasperini et al (2013) catalogs. The
 700 yellow stars represent the position of the 2019 Mw 6.0 Colfiorito and the Mw6.3 L'Aquila mainshocks.
 701 **B)** Mc-value time series using the same catalogs as A) and covering the periods between 1998 to 2009.
 702 The magnitude of completeness (Mc) varies in times from 2.5 (before 1997) to 1.4 (after 2005) with
 703 uncertainties δMc equals to 0.15 and 0.18 respectively. **C)** Temporal evolution of the G-R b-value in the
 704 central Appennines covering the same periods as in A. **D)** temporal evolution of the G-R b-value before
 705 and during the 1997 Colfiorito sequence. The b-value computation is resolved by using a coherent level
 706 of Mc equal to 2.5 ensuring a stable state over time and thereby minimizing b-value artifacts. The yellow
 707 star indicates the location of the Mw 6.0 event. It is worth noting that the trend observed in the b-value
 708 time series, as discussed in C), and incorporating temporal variations of Mc, closely mimic the results
 709 obtained when assuming a fixed Mc value of 2.5 and employing $N \sim 250$ fixed sample size windows with
 710 100 bootstraps.



712

713 **Figure 8** Temporal evolution of the G-R b-value (in red) and the cumulative number of
 714 earthquakes (in blue) during the Foreshock period priors to the Mw6.3 L'Aquila earthquake
 715 using the entire catalogs of Gasperini et al (2013). The b-value time series is obtained using a
 716 sample windows size of 150 events with 100 bootstraps. For safety, the M_c correction value is
 717 fixed at 0.2 comparable to the value used by the predictive foreshock model of Gulia et al
 718 (2016). The black stars represent the position of the Mw 6.3 L'Aquila mainshock.

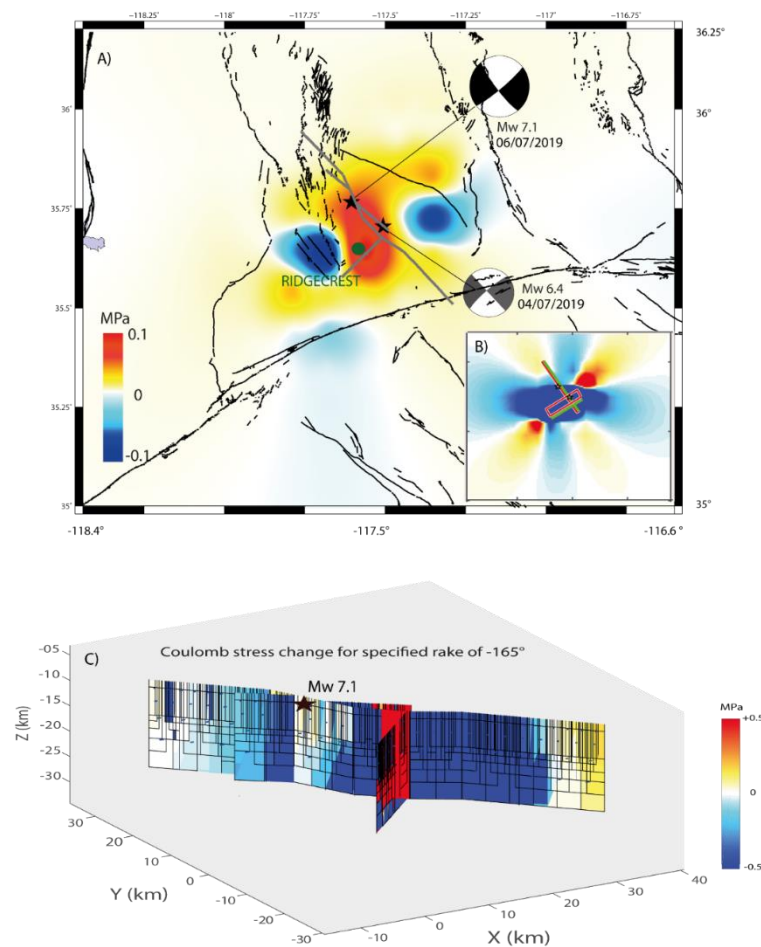
719 2. STRESS CHANGE, POROELASTICITY AND TEMPORAL EVOLUTION OF 720 AFTERSHOCK

721 As shown in the previous section, the occurrence of moderate to strong earthquakes along
 722 the SWL-ECSZ and Central Apennines zones may be coupled with the fluid migration along
 723 heterogeneous fault zones. This fluid migration can lead to abnormally elevated pore pressure
 724 and promote the occurrence of moderate to large earthquakes. Based on the Coulomb failure
 725 stress hypothesis, the post-seismic poroelastic stress change modeling following the Ridgecrest
 726 Mw 6.4 left-lateral event shows a high value of stress along the Mw7.1 right-lateral rupture

727 (Figures 9A and S13; Kariche, 2022) when the purely elastic stress modeling predicts an
728 absence of earthquake activities (Figures 9B and 9C; Lozos & Harris, 2020; Kariche, 2022).
729 The stress change modeling result in Figure 9A illustrates the post-seismic poroelastic stress
730 change scenario based on the assumption of cumulative poroelastic stress responses resulting
731 from changes in drained and undrained Poisson ratios. It also incorporates a significant
732 Skempton coefficient value ($B > 0.5$) (For a comprehensive understanding, refer to Section 3 of
733 "METHODOLOGY AND DATA" and Section 3 in Kariche, 2022). Subsequently, the study
734 compares the poroelastic stress response to the temporal evolution of poroelastic stress changes
735 that occurred following the Mw6.4 foreshock on the receiver fault plane responsible for the
736 Mw7.1 event. This comparison is made by employing different values of fluid diffusivity, as
737 depicted in Figure S13. The Coulomb stress change modeling (as illustrated in Figure S13)
738 considers a time-dependent pore-fluid pressure change derived from the solution proposed by
739 Piombo *et al.* (2005). In this modeling approach, a permeable source fault is assumed to be
740 associated with the Mw6.4 event. In contrast, the conjugated receiver fault plane in relation to
741 the Mw 7.1 nucleation area is considered as a barrier to the fluid flow.

742 Considering the diffusive effect of fluid, the Coulomb stress change modeling shows a
743 stress increase on the fault plane responsible for the Mw 7.1 earthquake (Figures 9A and S13C),
744 where the coseismic Coulomb stress change expects a negative (or insufficient) stress value
745 (Figures 9B and C). One of the possible explanations for the temporal evolution of stress change
746 values from negative to positive, as shown in Figures 9 and S13C, is the fluid redistribution
747 along conjugated fault ruptures, which creates favorable conditions for a weakening mechanism
748 by increasing pore-fluid pressure along the right-lateral fault rupture and, in fact, promoting the
749 occurrence of the Mw7.1 earthquake. The rupturing process on conjugated strike-slip faults
750 assisted by fluid migration is not unusual. Using a typical undrained and drained Poisson ratio
751 for a Berea sandstone, the modeling of the Coulomb failure function per unit of stress drop

752 caused by the 1987 Elmore Ranch event (Mw 6.2) on the conjugated Superstition Hills fault
753 (Mw 6.6) shows a maximum poroelastic stress value in the ~11 hr following the Mw 6.2 event
754 (Hudnut *et al.*, 1989). For the 2019 Ridgecrest sequence, the Coulomb stress change modeling,
755 taking into account the effect of fluids, reveals that the ~33 hr time delay between mainshocks
756 may be viewed as a triggering mechanism controlled by the fluid-flow process (Figures 9A and
757 S13; Kariche, 2022). The value of fluid diffusivity is relatively low compared to the value
758 obtained for the Superstition Hills sequence and may suggest that the fluid migration along
759 faults controls the delay between earthquakes. Note that the coseismic (undrained) isotropic
760 elastic stress change models, illustrated in Figures 9B and C, are undertaken primarily for
761 comparative purposes. They serve as a basis for comparison against the outcomes of short-term
762 poroelastic stress change modeling.



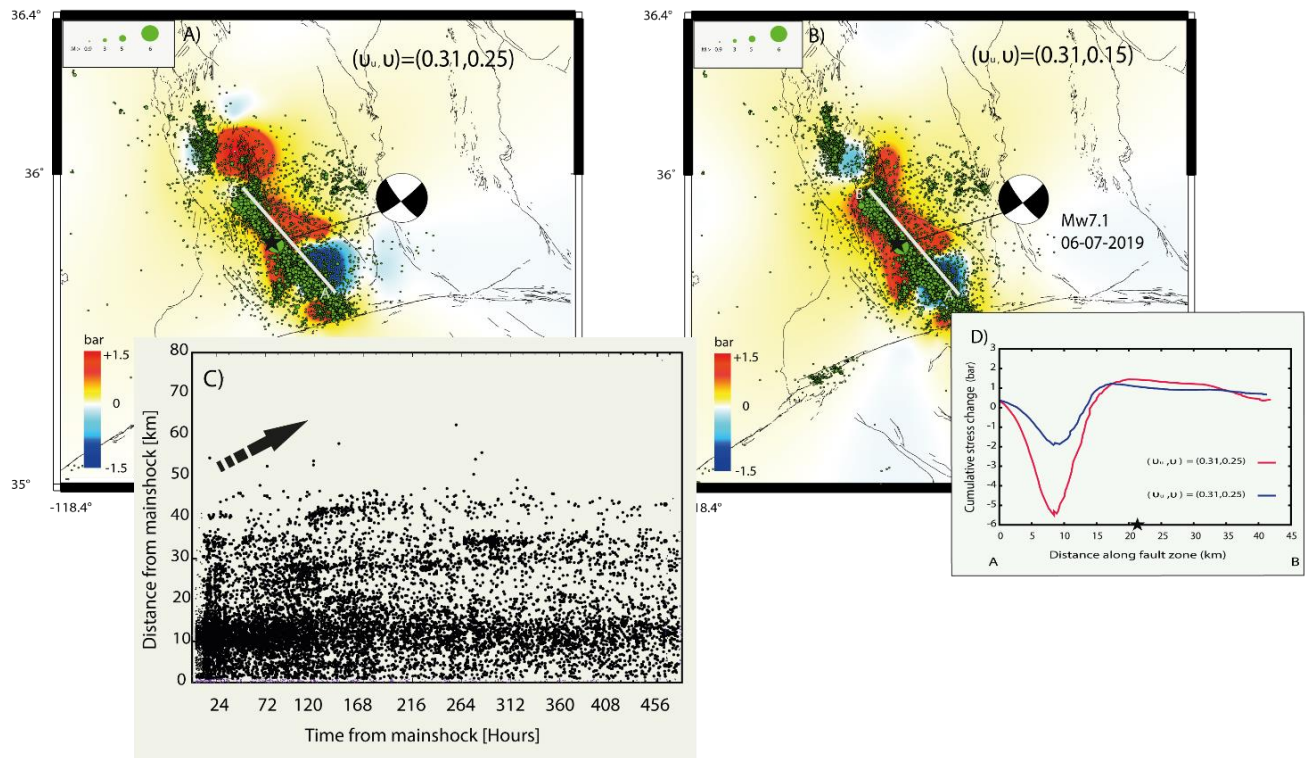
764 **Figure 9:** *A) Short-term poroelastic stress change modeling following the Mw6.4 earthquake*
765 *on receiver fault planes with Strike /Dip/ Rake = 143°/85°/-165° at 8km depth. The post-seismic*
766 *stress redistribution following the 04-07 (Mw6.4) from the undrained state to the drained fluid*
767 *state using extreme undrained and drained Poisson ration values ($\nu_u, \nu = 0.31, 0.15$). These*
768 *values are interpreted as a consequence of a high variation in rock rheology before and during*
769 *the Mw6.4 earthquake. The 2019 Ridgecrest surface rupture faults are from Xu et al (2020).*
770 *The grid depth is selected with respect to the Mw 7.1 hypocenter location of Wang et al., (2020).*
771 *B) Co seismic stress transfer caused by the Mw6.4 earthquake on receiver fault planes with*
772 *Strike /Dip/ Rake = 143°/85°/-165 at 8 km depth. The co-seismic stress modeling is performed*
773 *using simple conjugate fault geometries. C) Co-seismic stress change caused by the Mw 6.4 left*
774 *lateral rupture on the Mw 7.1 right lateral fault plane. The Mw 6.4 complex geometry and slip*
775 *distribution are from Xu et al (2020). The Coulomb stress change modeling was performed for*
776 *a fixed rake of -165° . The black star represents the same location of the Mw 7.1 event as in*
777 *figure 5.*

778 Fluid migration during an earthquake may also impact the frequency of aftershocks. Figure
779 10 illustrates the cumulative stress change modeling resulting from the complete poroelastic
780 relaxation of the Mw 7.1 Ridgecrest earthquake using different values of drained ν and
781 undrained ν_u Poisson ratios, in comparison to the spatial distribution of aftershocks following
782 the Mw7.1 Ridgecrest earthquake. Figures 10 (A, B, and C) reveal a correlation among: 1) the
783 evolution of stress change following the Mw 7.1 earthquake, 2) the fluid diffusion process, and
784 3) the spatial distribution of a subset of aftershocks near and NNW of the Mw7.1 epicenter. The
785 values of ν_u and ν used in Figure 10 might be associated with water-saturated rocks in the upper
786 few kilometers of the seismogenic zone ($h \leq 15$ km). The fluid-diffusion process within the
787 context of the 2019 Ridgecrest sequence appears to primarily operate at a local scale (Figures
788 9 and 10). The Coulomb stress change modeling, which incorporates the diffusive effects of

789 fluids, reveals a clear increase in stress change values near the epicentral region of the Mw 7.1
790 event (Figure 9A). Furthermore, the full poroelastic relaxation resulting from the Mw7.1 event,
791 particularly along faults parallel to the main rupture, seems to correspond to the spatial
792 distribution of aftershocks in the northern part of the Mw7.1 main rupture (Figures 10A, B, and
793 D).

794 In contrast, for the southern section of the Mw 7.1 Ridgecrest fault zone, the triggering
795 mechanism seems to operate independently of the fluid diffusion process (Figures 10A, B, C
796 and Figure S14). These findings support the idea that the generation of aftershocks following
797 the 2019 Ridgecrest earthquake is complex and may be related to both afterslip and poroelastic
798 relaxation processes. Indeed, an analysis of the co-seismic and early post-seismic surface
799 deformation (~2 months of deformation) following the 2019 Ridgecrest event suggests that the
800 observed post-seismic deformation during the first month may result from a combination of
801 afterslip and poroelastic rebound (Wang & Bürgmann, 2020). Based on the surface deformation
802 analysis (Wang & Bürgmann, 2020) and stress change modeling results (Figure 10), it is
803 reasonable to propose that the seismicity rate in the southern part of the Mw 7.1 main fault is
804 primarily driven by a model based on the evolution of afterslip, a conclusion supported by time
805 series analysis from the B921 strainmeter located in the same area (Hirakawa & Barbour, 2020).
806 Conversely, the early generation of aftershocks in the northern part appears to be predominantly
807 influenced by the poroelastic rebound resulting from the Mw 7.1 mainshock.

808 To explore the detailed mechanism of post-seismic deformation following the 2019
809 Ridgecrest sequence and related fluid migration, I analyze the temporal evolution of the
810 aftershock frequency rate associated with the Mw 7.1 earthquake and compare it with the case
811 of the Central Apennines. Figure 11 shows a comparison between the effect of fluid
812 redistribution on aftershock occurrence following the Mw 6.0 Colfiorito and the Mw 7.1
813 Ridgecrest earthquakes.



815

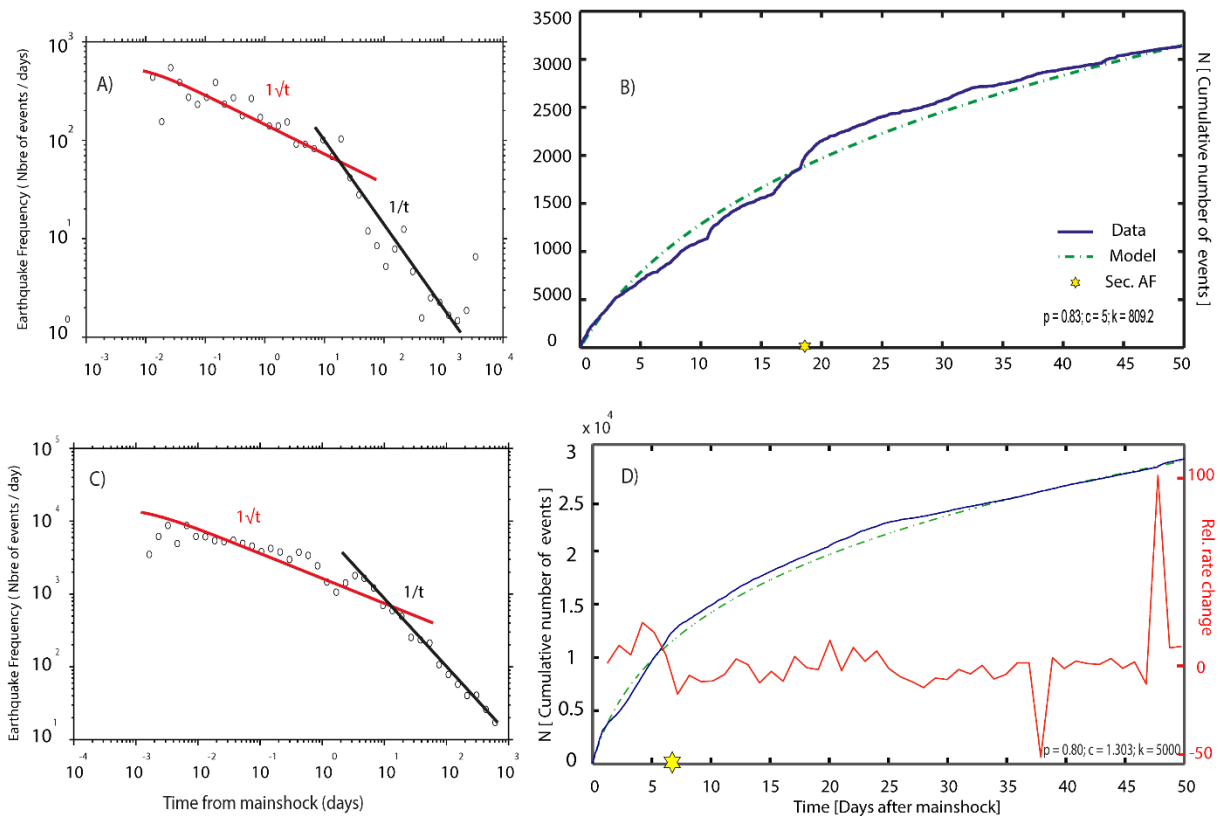
816 **Figure 10:** Cumulative stress change due to the full poroelastic rebound following the Mw7.1
 817 Ridgecrest earthquake on right lateral fixed receiver fault planes parallel to the Mw7.1 main rupture.
 818 A) poroelastic stress change modeling using a typical value of undrained and drained Poisson
 819 ratio $(\nu_u, \nu_v) = (0.31, 0.25)$. B) poroelastic stress change modeling using the extreme value of undrained
 820 and drained Poisson ratio $(\nu_u, \nu_v) = (0.31, 0.15)$. C) Spatiotemporal evolution of seismicity during the
 821 ~20 days following the Mw7.1 mainshock. The triggering front is represented as a time-distance
 822 plot of the events occurring from the Mw7.1 epicenter to the Coso geothermal area. D)
 823 Poroelastic stress change profiles caused by the full relaxation of the Mw7.1 earthquake along parallel
 824 right-lateral fault ruptures. The seismicity databases are from NEIC-USGS. The stress change modeling
 825 is fixed at 8 km depth. The black arrow in Figure C indicates the average direction of seismicity
 826 migration.

827 Figure 11 (A and C) shows strong similarities between the temporal evolution of the
 828 aftershock sequence following the two earthquakes. The aftershock frequency rate curve starts

829 with a rate decay of $1/\sqrt{t}$, while it becomes equal to $1/t$ in days to one month after the 1997
830 Colfiorito and Mw 7.1 Ridgecrest mainshocks as predicted by the pore-fluid diffusion equation
831 (see equation 8 in the methodology section; Figures 11A and C).

832 Based on the pore fluid flow hypothesis, the $1/\sqrt{t}$ decay is interpreted as an increase in
833 aftershock productivity due to the pore fluid diffusion along the fault zone. The increase in
834 aftershock productivity is also observed in Omori fit curve when the seismicity rate shows
835 additional aftershocks in the ~10–20 days after the Mw 6.0 Colfiorito and in the ~5–20 days
836 after the Mw 7.1 Ridgecrest mainshock (Figures 11B and D), which cannot be explained by the
837 aftershock rate decrease as predicted by the Omori Law. These results are also supported by the
838 abnormalities in aftershock activity observed during monitoring of the temporal and spatial
839 seismic activity following the Mw 6.4 Ridgecrest earthquake (Ogata & Omi, 2020). In addition,
840 the duration of the increase in aftershock activity (Figure 11D) seems to follow the duration of
841 pore-fluid instability as estimated by the b-value time series (Figure 4C). Note that the
842 underproduction of aftershocks as seen just after the Mw 7.1 mainshock (Figure 11C) may be
843 due to the under-reporting of small events in relation to the incompleteness of the seismic
844 catalogs soon after the mainshock.

845 The aftershock frequency rate curve (Figure 11A) also mimics the 1 km/day migration of
846 seismicity toward the southeast following the Mw 6.0 mainshock (Figure 1b in Catalli *et al.*,
847 2008). For the Ridgecrest sequence, the spatiotemporal analysis of the aftershocks indicates a
848 migration rate of ~4 km/day in the northern part of the Mw 7.1 event (Figure 10C, Figure 12).
849 Based on the pore pressure-diffusion propagation solution in an effective isotropic
850 homogeneous poroelastic medium (Shapiro, 2015, *Ch 3, Sect 3.3*), the shape of the pressure
851 front that best matches the 4 km/day aftershock migration rate is achieved by considering a high
852 fluid diffusivity value of 275 m²/s (Figure 12B).

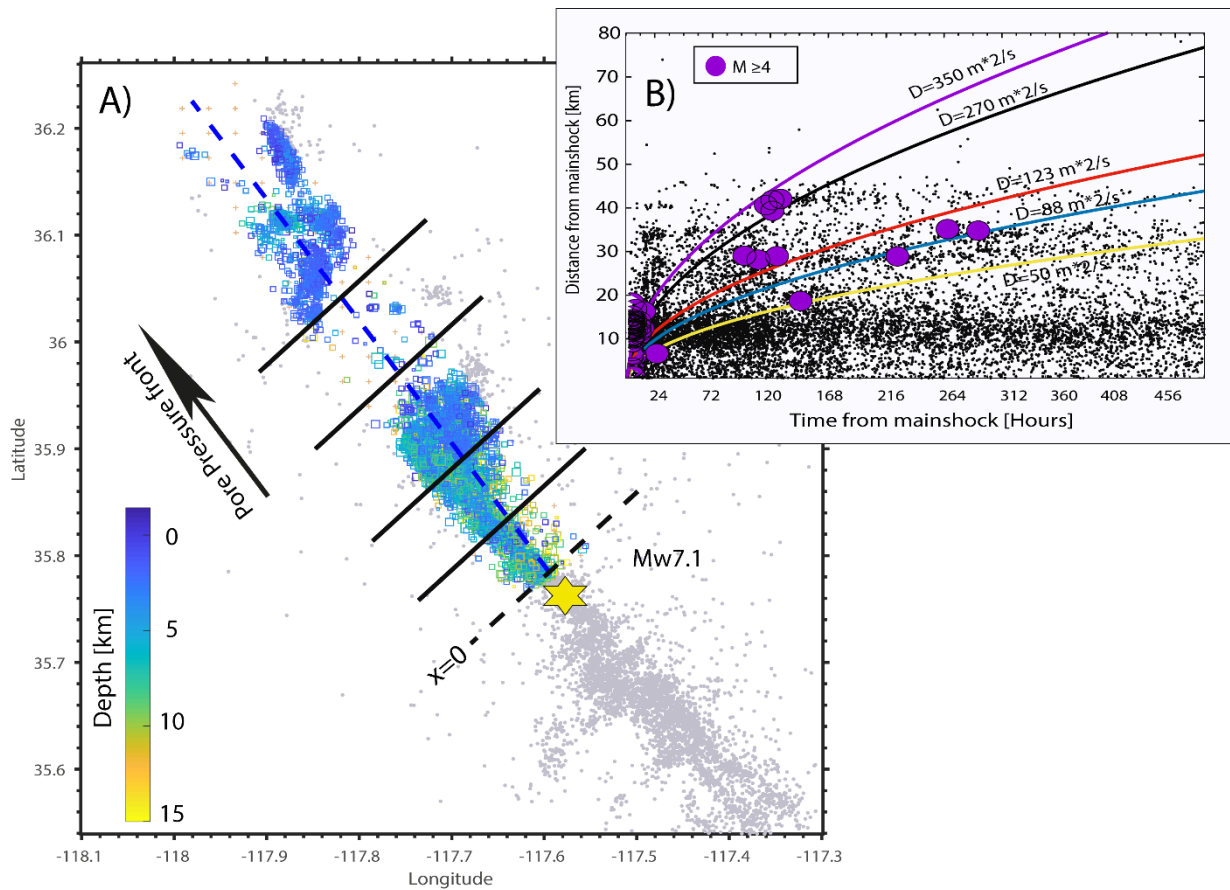


853

854 **Figure 11:** Representation of the temporal postseismic effect following the Mw 6.0 Colfiorito
 855 and Ridgecrest earthquakes. **A)** Seismicity rate change versus time following the Mw 6.0
 856 Colfiorito earthquake. **B)** Comparison of observed seismicity (blue) and the Omori fit (green)
 857 using the Zmap algorithm for 50 days' time windows following the Mw6.0 Colfiorito
 858 mainshock. **C)** Seismicity rate change versus time following the Mw 7.1 Ridgecrest earthquake.
 859 **D)** Comparison of observed seismicity (blue) and the Omori fit (green) following the Mw7.1
 860 Ridgecrest mainshock using the Zmap algorithm for 50 days' time windows. For the aftershock
 861 frequency vs time curves, the value of c is fixed to $0.01 d$ for Panels A and C and suppose
 862 variable (from 2.4 to 5) for Panels B and D. The yellow stars represent the position of the
 863 second major choc for each sequence. The relative earthquake rate change (red curve in D) is
 864 obtained from the change in slope of the cumulative number curve using a Habermann
 865 regardless of the time of greatest change and comparing the rate in the two parts of the period
 866 (before and after the division point) by fit-time windows function (Wyss & Habermann, 1988;

867 *Wyss & Wiemer 2000), the time variation function defines the variation between the rate before*
868 *and after at local time-scale.*

869 Despite that the migration rate associated with the Mw7.1 Ridgecrest aftershocks rate
870 appears to be slightly higher than that of the Colfiorito sequence, the fluid diffusivity value
871 obtained during the Mw 7.1 postseismic deformation phase (i.e. 275 m²/s) seems to be quite
872 similar to that observed for the entire Colfiorito sequence, taking into account the anisotropic
873 nature of fluid diffusivity (Antonioli *et al.*, 2005). Such a value of the fluid diffusivity is larger
874 than the 2.32 m²/s deduced from the poroelastic stress modeling imparted to the Mw 6.4
875 foreshock (Figure S13; Kariche, 2022) or obtained in the laboratory measurement for the same
876 lithologies. However, it is consistent with estimates of hydraulic diffusivity along Central
877 Italian active faults (Malagnini, 2012; Malagnini *et al.*, 2022), with in-situ measurements at the
878 Long Valley Caldera geothermal field (Roeloffs *et al.*, 2003), and with values deduced from
879 the analysis of induced seismicity due to wastewater injection in Western Oklahoma (Dempsey
880 & Riffault, 2019). Furthermore, using the poromechanical model of Byerlee (1993), I estimate
881 that permeability along the Ridgecrest fault zone increased by up to three orders of magnitude
882 (ranging from 10⁻¹¹ to 10⁻¹² m²) following the Mw 7.1 mainshock. This enhancement in
883 permeability is consistent with the inferred fluid diffusivity of 275 m²/s and reflects a significant
884 change in fault zone properties during the Mw 7.1 Ridgecrest earthquake.



885

886 **Figure 12:** *Spatiotemporal Evolution of Seismicity with $M \geq 2.5$ Following the Mw7.1*
 887 *Mainshock (~20 Days)* **A)** *Map showing seismic activity along the northern segment of the*
 888 *Mw7.1 Ridgecrest fault zone, which is used as input data for the pore fluid pressure diffusion*
 889 *modeling. The yellow star marks the epicenter of the Mw7.1 mainshock. Black lines represent*
 890 *the modeled pore pressure fronts. B)* *Time-distance plot of seismic events occurring in the*
 891 *northern segment of the Mw7.1 Ridgecrest fault zone. Events included in this plot were selected*
 892 *based on their location in the northern area of the Mw7.1 mainshock, as shown in A). The*
 893 *colored parabolic-like envelopes represent a linear diffusion-type approximation ($\sim \sqrt{t}$) of the*
 894 *triggering front. These triggering fronts are calculated using the pressure-diffusion*
 895 *propagation solution in an effective isotropic homogeneous poroelastic medium (Shapiro,*
 896 *2015, Ch.3, Sect.3.3). Fluid diffusivity values are determined for each distance-versus-time (r -*
 897 *t) plot with respect to the distribution of earthquakes with $M \geq 4$.*

898 DISCUSSION AND CONCLUSIONS

899 The high quality of the Southern California and Central Apennines earthquake catalogs
900 offers us the possibility to study in detail the evolution of seismicity and related fluid migration
901 at different time scales. The evolution of seismicity near Ridgecrest and the Central Apennines
902 reveals that the temporal variation in the b-value is probably due to the stress-fluid redistribution
903 along active faults. The b-value time series modeling shows a gradual decrease in the b-value
904 for all sequences. Based on previous laboratory experiment results on water-saturated
905 specimens (Main *et al.*, 1990; Sammonds *et al.*, 1992; Proctor *et al.*, 2020), the gradual decrease
906 in the b-value may be interpreted as a dilatancy softening mechanism caused by an increase in
907 pore fluid pressure before each seismic event. The remarkable similarities between the
908 evolution of the b-value following the 2019 Ridgecrest and the 2016 Amatrice-Norcia
909 sequences represented by two b-value minima are probably due to similarities in mechanisms
910 controlling the temporal evolution of foreshock-mainshock sequences. The duration of the first
911 b-value peak scales with the magnitude of the first foreshock while the duration of the second
912 peak (33 hr for Ridgecrest and 4 days for Amatrice-Norcia) appears to be independent of the
913 magnitude of related foreshocks-mainshocks. Based on the coupled b-value–stress intensity
914 laboratory experiments (eg. Sammonds *et al.*, 1992), the duration of the second peaks may be
915 interpreted as a short-term poroelastic stress redistribution following a fast slip episode. Also,
916 the temporal evolution of the b-value for the Ridgecrest and the Central Apennines fault zone
917 seems to be in good agreement with the fracture mechanics model of water-saturated specimens
918 as proposed by Main *et al.* (1989) who predict an increase in acoustic emission rate in the
919 dilatancy fluid diffusion phase when the static and dynamic stress drop are not necessarily
920 equal.

921 The idea that the fluids affect the change in the b-value is not necessarily contradicting the
922 explanation proposed by different authors that the b-value may act as a stress meter (e.g. Goebel

923 *et al.*, 2013; Scholz, 2015). The conceptual models proposed here suppose that the decrease in
924 the b-value before foreshock is followed by an acceleration in crack growth and eventually an
925 increase in differential stress over time. The only difference may relate to the modeling of the
926 stress evolution from the period between the foreshock and the mainshock, where the
927 acceleration of the crack front would be expected a decrease in elastic stress. At this time, the
928 decrease in elastic stress is compensated by the increase in pore fluid pressure in time and
929 therefore increases the Coulomb stress change on the receiver faults responsible for the large
930 rupturing process. In this study, the elevated pore-fluid pressure due to the fluid migration in
931 heterogeneous fault zone tends to affect the value of permeability and creates an area with a
932 low-stress drop tendency. Also, the occurrence of the Mw7.1 Ridgecrest right-lateral
933 earthquake is not necessarily associated with the presence of a large deep fluid reservoir. The
934 rapid fluctuation of the b-value just before the Mw7.1 may denote a rapid influx of fluid from
935 surrounding rocks, creating a pore fluid instability on nearby heterogeneous fault ruptures. The
936 temporal evolution of fault permeability and related pore-fluid diffusion appears to be a crucial
937 element in the apprehension of the difference in the time delay between earthquakes in the
938 Central Apennines and the SWL-ECSZ.

939 The interpretation presented in this study, based on the combined temporal evolution of
940 b-values and poromechanical processes, supports the role of complex fluid dynamics in
941 influencing foreshock behavior. Importantly, this perspective does not exclude the accelerating
942 moment release (AMR) hypothesis as a plausible explanation for moderate foreshock activity.
943 In the case of the 2009 L'Aquila sequence, the accelerating strain release (ASR) and pore fluid
944 diffusion (PFD) models likely represent complementary physical processes operating at
945 different spatial and temporal scales. The b-value time series presented here, which accounts
946 for fluid-related effects, is consistent with previous studies suggesting that multiple
947 mechanisms contributed to the preparatory phase of the L'Aquila earthquake. Supporting this

948 dual-process interpretation, Picozzi *et al.* (2022) reported that approximately one week before
949 the mainshock, the rupture initiation phase was characterized by elevated Energy Index (EI)
950 values, indicative of enhanced slip per unit stress. This behavior correlates with a concurrent
951 drop in b-values and lends mechanical support to the model of overpressurized fluid diffusion
952 into the fault zone. As the foreshock sequence progressed, the temporal evolution of dynamic
953 source parameters revealed a transition toward strain-controlled rupture nucleation. These
954 findings support a complex, hybrid preparatory model in which early-stage fluid overpressure
955 facilitates fault weakening and nucleation, while progressive tectonic stress accumulation
956 ultimately drives the Mw 6.3 L'Aquila mainshock.

957 In the same register, Gulia *et al.* (2020) developed a real-time earthquake monitoring
958 system based on a traffic–light classification that uses the temporal change in b-value to
959 constrain whether an ongoing earthquake sequence represents a decaying aftershock phase or
960 precursors to an upcoming large event. Dascher-Cousineau *et al.* (2020) published a paper that
961 points out that the methodology proposed by Gulia *et al.* (2020) gives results in terms of
962 evaluating the risk of a large impending earthquake during the Mw 6.4 Ridgecrest foreshock,
963 this method fails to predict the onset of the Mw 7.1 sequence. Also, Dascher-Cousineau *et al.*
964 (2020) show that for the case of the 2019 Ridgecrest sequence, anomalous earthquake
965 productivity in adjacent regions may affect the background b-values and generate a false alarm.
966 In this study, the b-value time series interpretation taking into account the poroelastic properties
967 of the seismogenic zone shows difficulties to establish a good correlation between the duration
968 of the foreshock activities and the magnitude of the next largest expected earthquake. Despite
969 the fact that the inverse dependency of the b-value and the applied stress appears to be a
970 reasonable interpretation of the b-value drop prior to the Italian and Californian sequences
971 (Gulia & Wiemer, 2019; Gulia *et al.* 2020; Figure S13), the fluctuations of the b-value following
972 the 2019 Ridgecrest and 2016 Amatrice foreshock sequences characterized by a double

973 minimum seem to unfollow the hypothesis that the drop in the b-value before mainshocks is
974 only due to the presence of high-stress levels on receiver main ruptures. This may suggest that
975 the magnitude of the large expected earthquake is controlled by the variations in pore-fluid
976 pressure rather than the maximum differential stress.

977 In the case of immature faults as for the 2019 Ridgecrest earthquake sequence, fluctuations
978 in fluid mass balance can induce significant dilatancy effects. These effects, in turn, impact the
979 evolution of pore-fluid pressure along the fault and could potentially directly influence the
980 dynamic strength of the fault. Mechanically, the pore pressure drop during the dilatancy phase
981 would be recovered at a short time scale by increasing pore-fluid pressure due to the fluid
982 redistribution along the shear zone. If we assume that fault slip is governed by the balance
983 between the frictional strength and the shear stress acting on a fault (Segall & Rice, 1995;
984 Heimisson *et al.*, 2022), the increase in pore-fluid pressure tends to reduce the effective normal
985 stress along the receiver fault. Consequently, this increase in pore fluid pressure can lead to an
986 accelerated slip rate, thereby affecting the size of earthquakes.

987 The physics model of aftershock occurrence as proposed in this paper and based on the
988 dilatancy-diffusion hypothesis validates the assumption that a part of the production of
989 aftershocks is intimately linked to the fluid flow diffusion process. The $1/\sqrt{t}$ rate decay in the
990 aftershock's activity observed in the days following the Mw 6.0 Colfiorito and the Mw 7.1
991 Ridgecrest mainshocks is interpreted as an increase in aftershock productivity due to the pore
992 fluid diffusion along the Colfiorito and Ridgecrest fault zones. The seismicity distribution for
993 extensional earthquakes in Central Apennines shows a seismic migration velocity of 1-3.5
994 km/day during the mainshock-aftershock sequence that indicates a high fluid diffusivity ranging
995 from 60-2000m²/s (Catalli *et al.*, 2008; Lombardi *et al.*, 2010; Chiaraluce, 2012; Malagnini *et*
996 *al.*, 2022). Spatiotemporal analysis of the Ridgecrest aftershock sequence reveals that the short-
997 term seismicity migration along the northern part of the Mw7.1 earthquake occurs at a rate of

998 approximately 4 km/day with an apparent fluid diffusivity ranging from 50-270 m²/s. This rate
999 is consistent with those observed in Central Apennines, suggesting significant fluid drainage
1000 contributing to aftershock productivity.

1001 The kinematic and physical properties of the fault zone may explain the substantial
1002 differences in fluid diffusivity before and after the Mw 7.1 Ridgecrest main event. The low
1003 fluid diffusivity obtained during the Mw 6.4 foreshock sequence is explained by the poroelastic
1004 stress mechanism used in the modeling of fault interactions, which account for stress-fluid
1005 interactions. This low diffusivity value suggests that fluid drainage is limited by the anisotropy
1006 of the fault zone permeability where the Mw 6.4 conjugated right-lateral rupture acts as a fluid
1007 barrier. In this scenario, the poroelastic properties of the seismogenic zone led to elevated pore
1008 fluid pressure, affecting the effective normal stress on the delayed Mw 7.1 fault rupture. Thus,
1009 the Mw 6.4 foreshock sequence may be seen as a poroelastic undrained-drained preparatory
1010 phase that precedes the larger Mw 7.1 event. The significant dilatancy effect during the
1011 coseismic phase of the Mw 7.1 earthquake tends to drastically increase fault zone permeability,
1012 thereby facilitating fluid drainage. This implies that, during the Mw 7.1-early aftershock period,
1013 the Ridgecrest fault zone acts as a "fluid drainage channel". Consequently, the high fluid flow
1014 resulting from the change in permeability generates a large pore pressure front that affects the
1015 aftershock behavior.

1016 The analysis of the spatiotemporal evolution of seismicity combined with the results of
1017 poroelastic stress change as presented in this study testifies that a large portion of aftershocks
1018 occurred within fluid-saturated regions largely decoupled from both shallow and deep afterslip
1019 patches as identified in geodetic models (Pollitz et al., 2022; He et al., 2022; Yue et al., 2021;
1020 Qiu et al., 2020). These afterslip zones are typically associated with rate-strengthening frictional
1021 behavior, where deformation is accommodated aseismically through stable sliding. Moreover,
1022 near-field GNSS stations located in the northwestern portion of the Mw 7.1 rupture zone

1023 recorded fault-normal displacements consistent with early InSAR observations (Brooks et al.,
1024 2020; Wang & Bürgmann, 2020), suggesting that poroelastic rebound, rather than afterslip,
1025 dominated the early postseismic deformation. In contrast, the southern Mw 7.1 fault exhibits a
1026 distinctly different postseismic signature. Stress change modeling indicates that poroelastic
1027 stress changes in this area had a predominantly negative (inhibitive) effect on fault failure, and
1028 fluid diffusion processes appear to be absent or negligible. Instead, borehole strainmeters
1029 located in this zone reveal a strong and spatially focused afterslip signal (Hirakawa & Barbour,
1030 2020; Hanagan et al., 2024), suggesting that afterslip played a more dominant role.

1031 The spatiotemporal distribution of aftershocks following the 2019 Ridgecrest earthquake
1032 is complex (Ross *et al.* 2019; Trugman, 2020). The complex slip distribution and the
1033 heterogeneity in fault zone tend to maintain elevated fluid pressure and in fact, increase
1034 aftershock productivity. The analysis of seismicity shows that the concentration of seismicity
1035 immediately after the Mw 7.1 shut down along the Mw 6.4 conjugated rupture and therefore
1036 the aftershock distribution was mainly concentrated along the Mw 7.1 right-lateral fault plane
1037 (Toda & Stein, 2020). This observation supports the idea that in general, the fluid migrates
1038 linearly at a short-time scale and suppresses the possibility that the fluid flows out of local high-
1039 pressure compartments just after the occurrence of the Mw 7.1 mainshock. However,
1040 complexity in the slip distribution and geometry of fault rupture may perturb the fluid pressure
1041 distribution and give rise to a heterogeneous fluid-flow process at a local scale. At this time,
1042 more detailed aftershock modeling procedures (e.g., Yamashita & Tsutsumi, 2018, Sect. 6.3)
1043 may be included to give a complete estimation of the complex fluid-flow process. Note that
1044 these results are also valid for the Central Apennines sequences.

1045 A more complete 3-D pore-pressure analysis and a careful analysis of the spatiotemporal
1046 evolution of stress drop along active faults may mimic the level of effective stress before,
1047 during, and after major earthquake sequences. This approach may yield a more accurate

1048 estimation of the evolution of the fluid-flow processes within active fault zones. Based on our
1049 results, detailed knowledge of geological structures, substratum permeability, and a robust
1050 evaluation of the pore fluid effect with a better constrain of seismicity and strain rate before and
1051 during seismic sequences combined with a more complete physics-based and statistical forecast
1052 methods appears to be fundamental for the seismic hazard assessment and any decision making.

1053 **DATA AVAILABILITY STATEMENTS**

1054 The global earthquake catalogs can be downloaded from the Istituto Nazionale Di Geofisica E
1055 Vulcanology (INGV) at <http://terremoti.ingv.it/en> and the U.S. Geological Survey (USGS-
1056 NEIC) at <https://earthquake.usgs.gov/earthquakes/search/>. The earthquake focal mechanisms
1057 were obtained through the Global Centroid Moment Tensor solutions available at
1058 <https://www.globalcmt.org/CMTsearch.html>. The Quake Template Matching (QTM) catalog
1059 for Southern California, necessary to produce the Ridgecrest time series, was acquired from
1060 Ross et al. (2019) in its original form at <https://scedc.caltech.edu/data/qtm-catalog.html>. The
1061 QTM catalog was combined with the higher-resolution Ridgecrest datasets from Shelly (2020),
1062 available at <https://www.sciencebase.gov/catalog/item/5dd715f3e4b0695797650d18>. The Tan
1063 et al (2021) catalog used in the b-value time series can be found in the Zenodo dataset repository
1064 (<https://zenodo.org/records/4662870>). The Mw7.1 Ridgecrest source time function can be
1065 downloaded from IRIS at <https://ds.iris.edu/spud/momenttensor>. The Xu et al (2020) Ridgecrest
1066 fault slip model was downloaded in its original form from the SRCMOD project (<http://equake-rc.info/srcmod/>).
1067 The converted Matlab format, necessary for performing the stress change
1068 modeling, is available through the Zenodo platform at <https://zenodo.org/records/10029978>.
1069 All datasets required to reproduce the b-value time series and stress change modeling in
1070 connection with this study are available in Matlab and Coulomb input formats at
1071 <https://zenodo.org/records/10029978>.

1072 **ACKNOWLEDGMENTS**

1073 The author wishes to express sincere gratitude to M. Meghraoui (ITES, University of
1074 Strasbourg) and R. Toussaint (ITES, University of Strasbourg) for insightful discussions on the
1075 conceptual framework of stress transfer and poroelastic deformation. Special thanks are
1076 extended to Andrew J. Barbour (USGS) and Teruo Yamashita (The University of Tokyo) for
1077 their careful review of an earlier version of the manuscript and for their valuable suggestions
1078 and comments. The author is equally grateful to the anonymous reviewer for their thorough
1079 evaluation and constructive feedback, and to the Editor, Maurizio Ripepe, for his technical
1080 support throughout the review process. This research was supported by the Direction of
1081 Research at MESRS (Algeria) and the Direction Europe de la Recherche et Coopération
1082 Internationale (DERCI-CNRS). Several figures were prepared using the public-domain Generic
1083 Mapping Tools (GMT) software (Wessel & Smith, 1998).

1084 **DECLARATION OF COMPETING INTEREST**

1085 The author confirms that he has no competing financial interests or personal relationships that
1086 could have influenced the work reported in this paper.

1087 **REFERENCES**

- 1088 Abramowitz, M., & Stegun, I. (1970). Dover. *Handbook of mathematical functions*.
- 1089 Aki, K. (1965). Maximum likelihood estimate of b in the formula $\log N = a - bM$ and its
1090 confidence limits. *Bull. Earthq. Res. Inst., Tokyo Univ.*, 43, 237-239.
- 1091 Amato, A., Azzara, R., Chiarabba, C., Cimini, G., Cocco, M., Di Bona, M., Margheriti, L.,
1092 Mazza, S., Mele, F., & Selvaggi, G. (1998). The 1997 Umbria-Marche, Italy, earthquake
1093 sequence: A first look at the main shocks and aftershocks. *Geophysical Research*
1094 *Letters*, 25(15), 2861-2864.

1095 Antoine, S. L., Klinger, Y., Delorme, A., Wang, K., Bürgmann, R., & Gold, R. D. (2021).
1096 Diffuse deformation and surface faulting distribution from submetric image correlation
1097 along the 2019 Ridgecrest, California, ruptures. *Bull. Seismol. Soc. Am.*, 5, 2275-2302.

1098 Antonioli, A., Piccinini, D., Chiaraluce, L., & Cocco, M. (2005). Fluid flow and seismicity
1099 pattern : Evidence from the 1997 Umbria-Marche (central Italy) seismic sequence.
1100 *Geophysical Research Letters*, 32(10).

1101 Axen, G. J. (1992). Pore pressure, stress increase, and fault weakening in low-angle normal
1102 faulting. *Journal of Geophysical Research*, 97(B6), 8979.
1103 <https://doi.org/10.1029/92JB00517>

1104 Barnhart, W. D., Hayes, G. P., & Gold, R. D. (2019). The July 2019 Ridgecrest, California
1105 Earthquake Sequence : Kinematics of Slip and Stressing in Cross-Fault Ruptures.
1106 *Geophysical Research Letters*, 0(ja). <https://doi.org/10.1029/2019GL084741>

1107 Beeler, N., Simpson, R., Hickman, S., & Lockner, D. (2000). Pore fluid pressure, apparent
1108 friction, and Coulomb failure. *Journal of Geophysical Research: Solid Earth*, 105(B11),
1109 25533-25542.

1110 Berg, E. (1968). Relation between earthquake foreshocks, stress and mainshocks. *Nature*,
1111 219(5159), 1141-1143.

1112 Biot, M. A. (1965). *Mechanics of incremental deformations*.

1113 Booker, J. R. (1974). Time dependent strain following faulting of a porous medium. *Journal of*
1114 *Geophysical Research*, 79(14), 2037-2044.

1115 Bosl, W., & Nur, A. (2002). Aftershocks and pore fluid diffusion following the 1992 Landers
1116 earthquake. *Journal of Geophysical Research: Solid Earth*, 107(B12), ESE-17.

1117 Brantut, N. (2020). Dilatancy-induced fluid pressure drop during dynamic rupture : Direct
1118 experimental evidence and consequences for earthquake dynamics. *Earth and Planetary*
1119 *Science Letters*, 538, 116179. <https://doi.org/10.1016/j.epsl.2020.116179>

1120 Brooks, B. A., Murray, J., Svarc, J., Phillips, E., Turner, R., Murray, M., Ericksen, T., Wang,
1121 K., Minson, S., & Burgmann, R. (2020). Rapid geodetic observations of
1122 spatiotemporally varying postseismic deformation following the Ridgecrest earthquake
1123 sequence : The US Geological Survey response. *Seismological Research Letters*, *91*(4),
1124 2108-2123.

1125 Byerlee, J. D. (1993). Model for episodic flow of high-pressure water in fault zones before
1126 earthquakes. *Geology*, *21*(4), 303-306.

1127 Cappa, F., Scuderi, M. M., Collettini, C., Guglielmi, Y., & Avouac, J.-P. (2019). Stabilization
1128 of fault slip by fluid injection in the laboratory and in situ. *Science advances*, *5*(3),
1129 eaau4065.

1130 Catalli, F., Cocco, M., Console, R., & Chiaraluca, L. (2008). Modeling seismicity rate changes
1131 during the 1997 Umbria-Marche sequence (central Italy) through a rate- and state-
1132 dependent model. *Journal of Geophysical Research: Solid Earth*, *113*(B11),
1133 2007JB005356. <https://doi.org/10.1029/2007JB005356>

1134 Chambon, G., & Rudnicki, J. W. (2001). Effects of normal stress variations on frictional
1135 stability of a fluid-infiltrated fault. *Journal of Geophysical Research: Solid Earth*,
1136 *106*(B6), 11353-11372.

1137 Cheloni, D., De Novellis, V., Albano, M., Antonioli, A., Anzidei, M., Atzori, S., Avallone, A.,
1138 Bignami, C., Bonano, M., Calcaterra, S., Castaldo, R., Casu, F., Cecere, G., De Luca,
1139 C., Devoti, R., Di Bucci, D., Esposito, A., Galvani, A., Gambino, P., ... Doglioni, C.
1140 (2017). Geodetic model of the 2016 Central Italy earthquake sequence inferred from
1141 InSAR and GPS data. *Geophysical Research Letters*, *44*(13), 6778-6787.
1142 <https://doi.org/10.1002/2017GL073580>

1143 Chen, C.-T., Chan, Y.-C., Beyssac, O., Lu, C.-Y., Chen, Y.-G., Malavieille, J., Kidder, S. B.,
1144 & Sun, H.-C. (2019). Thermal History of the Northern Taiwanese Slate Belt and

1145 Implications for Wedge Growth During the Neogene Arc-Continent Collision.
1146 *Tectonics*, 38(9), 3335-3350. <https://doi.org/10.1029/2019TC005604>

1147 Chiarabba, C., Buttinelli, M., Cattaneo, M., & De Gori, P. (2020). Large earthquakes driven by
1148 fluid overpressure : The Apennines normal faulting system case. *Tectonics*, 39(4),
1149 e2019TC006014.

1150 Chiaraluce, L., Ellsworth, W., Chiarabba, C., & Cocco, M. (2003). Imaging the complexity of
1151 an active normal fault system : The 1997 Colfiorito (central Italy) case study. *Journal*
1152 *of Geophysical Research: Solid Earth*, 108(B6).

1153 Chiodini, G., Cardellini, C., Amato, A., Boschi, E., Caliro, S., Frondini, F., & Ventura, G.
1154 (2004). Carbon dioxide Earth degassing and seismogenesis in central and southern Italy.
1155 *Geophysical Research Letters*, 31(7).

1156 Cocco, M., & Rice, J. R. (2002). Pore pressure and poroelasticity effects in Coulomb stress
1157 analysis of earthquake interactions. *Journal of Geophysical Research: Solid Earth*,
1158 107(B2), ESE-2.

1159 Combs, J. (1980). Heat flow in the Coso Geothermal Area, Inyo County, California. *Journal of*
1160 *Geophysical Research*, 85(B5), 2411. <https://doi.org/10.1029/JB085iB05p02411>

1161 Dascher-Cousineau, K., Lay, T., & Brodsky, E. E. (2020). Two foreshock sequences post Gulia
1162 and Wiemer (2019). *Seismological Society of America*, 91(5), 2843-2850.

1163 De Barros, L., Cappa, F., Deschamps, A., & Dublanchet, P. (2020). Imbricated aseismic slip
1164 and fluid diffusion drive a seismic swarm in the Corinth Gulf, Greece. *Geophysical*
1165 *Research Letters*, 47(9), e2020GL087142.

1166 Dempsey, D., & Riffault, J. (2019). Response of induced seismicity to injection rate reduction :
1167 Models of delay, decay, quiescence, recovery, and Oklahoma. *Water Resources*
1168 *Research*, 55(1), 656-681.

1169 Deschamps, A., Courboux, F., Gaffet, S., Lomax, A., Virieux, J., Amato, A., Azzara, A.,
1170 Castello, B., Chiarabba, C., & Cimini, G. (2000). Spatio-temporal distribution of
1171 seismic activity during the Umbria-Marche crisis, 1997. *Journal of Seismology*, 4(4),
1172 377-386.

1173 Ekström, G., Morelli, A., Boschi, E., & Dziewonski, A. M. (1998). Moment tensor analysis of
1174 the central Italy earthquake sequence of September–October 1997. *Geophysical
1175 Research Letters*, 25(11), 1971-1974.

1176 Enescu, B., Mori, J., & Miyazawa, M. (2007). Quantifying early aftershock activity of the 2004
1177 mid-Niigata Prefecture earthquake (Mw6.6). *Journal of Geophysical Research: Solid
1178 Earth*, 112(B4). <https://doi.org/10.1029/2006JB004629>

1179 Fielding, E. J., Liu, Z., Stephenson, O. L., Zhong, M., Liang, C., Moore, A., Yun, S., & Simons,
1180 M. (2020). Surface Deformation Related to the 2019 M w 7.1 and 6.4 Ridgecrest
1181 Earthquakes in California from GPS, SAR Interferometry, and SAR Pixel Offsets.
1182 *Seismological Research Letters*.

1183 Gardner, J., & Knopoff, L. (1974). Is the sequence of earthquakes in Southern California, with
1184 aftershocks removed, Poissonian? *Bulletin of the seismological society of America*,
1185 64(5), 1363-1367.

1186 Gasperini, P., Lolli, B., & Vannucci, G. (2013). Empirical calibration of local magnitude data
1187 sets versus moment magnitude in Italy. *Bulletin of the Seismological Society of America*,
1188 103(4), 2227-2246.

1189 Goebel, T. H. W., Schorlemmer, D., Becker, T. W., Dresen, G., & Sammis, C. G. (2013).
1190 Acoustic emissions document stress changes over many seismic cycles in stick-slip
1191 experiments. *Geophysical Research Letters*, 40(10), 2049-2054.
1192 <https://doi.org/10.1002/grl.50507>

- 1193 Gulia, L., Tormann, T., Wiemer, S., Herrmann, M., & Seif, S. (2016). Short-term probabilistic
1194 earthquake risk assessment considering time-dependent b values. *Geophysical Research*
1195 *Letters*, 43(3), 1100-1108. <https://doi.org/10.1002/2015GL066686>
- 1196 Gulia, L., & Wiemer, S. (2019). Real-time discrimination of earthquake foreshocks and
1197 aftershocks. *Nature*, 574(7777), 193-199.
- 1198 Gulia, L., Wiemer, S., & Vannucci, G. (2020). Pseudoprospective Evaluation of the Foreshock
1199 Traffic-Light System in Ridgecrest and Implications for Aftershock Hazard
1200 Assessment. *Seismological Society of America*, 91(5), 2828-2842.
- 1201 Guo, Z., & Ogata, Y. (1997). Statistical relations between the parameters of aftershocks in time,
1202 space, and magnitude. *Journal of Geophysical Research: Solid Earth*, 102(B2),
1203 2857-2873.
- 1204 Gutenberg, G., & Richter, C. (1950). Seismicity of the earth and associated phenomena,
1205 Howard Tatel. *JGR*, 55, 97.
- 1206 Hanagan, C., Bennett, R. A., Barbour, A., & Hughes, A. N. (2024). Afterslip and Creep in the
1207 Rate-Dependent Framework: Joint Inversion of Borehole Strain and GNSS
1208 Displacements for the Mw 7.1 Ridgecrest Earthquake. *Journal of Geophysical*
1209 *Research: Solid Earth*, 129(10), e2024JB028908.
1210 <https://doi.org/10.1029/2024JB028908>
- 1211 Hauksson, E., Hutton, K., Kanamori, H., Jones, L., Mori, J., Hough, S., & Roquemore, G.
1212 (1995). Preliminary Report on the 1995 Ridgecrest Earthquake Sequence in Eastern
1213 California. *Seismological Research Letters*, 66(6), 54-60.
1214 <https://doi.org/10.1785/gssrl.66.6.54>
- 1215 He, K., Xu, C., & Wen, Y. (2022). Coseismic and early post-seismic deformations due to the
1216 2019 earthquake sequence in Ridgecrest, California. *Geophysical Journal International*,
1217 230(2), 957-975. <https://doi.org/10.1093/gji/ggac103>

- 1218 Heimisson, E. R., Liu, S., Lapusta, N., & Rudnicki, J. (2022). A Spectral Boundary-Integral
1219 Method for Faults and Fractures in a Poroelastic Solid : Simulations of a Rate-and-State
1220 Fault With Dilatancy, Compaction, and Fluid Injection. *Journal of Geophysical
1221 Research: Solid Earth*, *127*(9), e2022JB024185.
- 1222 Hickman, S., Sibson, R., & Bruhn, R. (1995). Introduction to special section : Mechanical
1223 involvement of fluids in faulting. *Journal of Geophysical Research: Solid Earth*,
1224 *100*(B7), 12831-12840.
- 1225 Hirakawa, E., & Barbour, A. J. (2020). Kinematic Rupture and 3D Wave Propagation
1226 Simulations of the 2019 Mw 7.1 Ridgecrest, California, Earthquake. *Bulletin of the
1227 Seismological Society of America*, *110*(4), 1644-1659.
1228 <https://doi.org/10.1785/0120200031>
- 1229 Hudnut, K. W., Seeber, L., & Pacheco, J. (1989). Cross-fault triggering in the November 1987
1230 Superstition Hills earthquake sequence, southern California. *Geophysical Research
1231 Letters*, *16*(2), 199-202.
- 1232 Kariche, J. (2022). The 2020 Monte Cristo (Nevada) Earthquake Sequence : Stress Transfer in
1233 the Context of Conjugate Strike-Slip Faults. *Tectonics*, *41*(3), e2020TC006506.
- 1234 Kariche, J., Meghraoui, M., Timoulali, Y., Cetin, E., & Toussaint, R. (2018). The Al Hoceima
1235 earthquake sequence of 1994, 2004 and 2016 : Stress transfer and poroelasticity in the
1236 Rif and Alboran Sea region. *Geophysical Journal International*, *212*(1), 42-53.
1237 <https://doi.org/10.1093/gji/ggx385>
- 1238 Khoshmanesh, M., & Shirzaei, M. (2018). Episodic creep events on the San Andreas Fault
1239 caused by pore pressure variations. *Nature geoscience*, *11*(8), 610.
- 1240 Kirkpatrick, J., Shipton, Z., Evans, J. P., Micklethwaite, S., Lim, S., & McKillop, P. (2008).
1241 Strike-slip fault terminations at seismogenic depths : The structure and kinematics of

1242 the Glacier Lakes fault, Sierra Nevada United States. *Journal of Geophysical Research:*
1243 *Solid Earth*, 113(B4).

1244 Lombardi, A. M., Cocco, M., & Marzocchi, W. (2010). On the Increase of Background
1245 Seismicity Rate during the 1997-1998 Umbria-Marche, Central Italy, Sequence :
1246 Apparent Variation or Fluid-Driven Triggering? *Bulletin of the Seismological Society*
1247 *of America*, 100(3), 1138-1152. <https://doi.org/10.1785/0120090077>

1248 Main, I. G., Meredith, P. G., & Jones, C. (1989). A reinterpretation of the precursory seismic
1249 b-value anomaly from fracture mechanics. *Geophysical Journal International*, 96(1),
1250 131-138.

1251 Main, I. G., Meredith, P. G., Sammonds, P. R., & Jones, C. (1990). Influence of fractal flaw
1252 distributions on rock deformation in the brittle field. *Geological Society, London,*
1253 *Special Publications*, 54(1), 81-96.

1254 Malagnini, L., Lucente, F. P., De Gori, P., Akinci, A., & Munafo', I. (2012). Control of pore
1255 fluid pressure diffusion on fault failure mode : Insights from the 2009 L'Aquila seismic
1256 sequence. *Journal of Geophysical Research: Solid Earth*, 117(B5).

1257 Malagnini, L., Parsons, T., Munafò, I., Mancini, S., Segou, M., & Geist, E. L. (2022). Crustal
1258 permeability changes inferred from seismic attenuation : Impacts on multi-mainshock
1259 sequences. *Frontiers in Earth Science*, 10, 963689.
1260 <https://doi.org/10.3389/feart.2022.963689>

1261 Miller, S. A. (2020). Aftershocks are fluid-driven and decay rates controlled by permeability
1262 dynamics. *Nature communications*, 11(1), 1-11.

1263 Monastero, F. C., Walker, J. D., Katzenstein, A. M., Sabin, A. E., Glazner, A., & Bartley, J.
1264 (2002). Neogene evolution of the Indian Wells Valley, east-central California. *Geologic*
1265 *evolution of the Mojave Desert and southwestern Basin and Range: Geological Society*
1266 *of America Memoir*, 195, 199-228.

1267 Moro, M., Saroli, M., Stramondo, S., Bignami, C., Albano, M., Falcucci, E., Gori, S., Doglioni,
1268 C., Polcari, M., & Tallini, M. (2017). New insights into earthquake precursors from
1269 InSAR. *Scientific reports*, 7(1), 12035.

1270 Nanjo, K., Hirata, N., Obara, K., & Kasahara, K. (2012). Decade-scale decrease in b value prior
1271 to the M9-class 2011 Tohoku and 2004 Sumatra quakes. *Geophysical Research Letters*,
1272 39(20).

1273 Nespoli, M., Belardinelli, M. E., Gualandi, A., Serpelloni, E., & Bonafede, M. (2018).
1274 Poroelasticity and Fluid Flow Modeling for the 2012 Emilia-Romagna Earthquakes :
1275 Hints from GPS and InSAR Data. *Geofluids*, 2018.

1276 Nur, A., & Booker, J. R. (1972). Aftershocks caused by pore fluid flow? *Science*, 175(4024),
1277 885-887.

1278 Picozzi, M., Spallarossa, D., Iaccarino, A. G., & Bindi, D. (2022). Temporal Evolution of
1279 Radiated Energy to Seismic Moment Scaling During the Preparatory Phase of the Mw
1280 6.1, 2009 L'Aquila Earthquake (Italy). *Geophysical Research Letters*, 49(8),
1281 e2021GL097382. <https://doi.org/10.1029/2021GL097382>

1282 Pino, N. A., Convertito, V., & Madariaga, R. (2019). Clock advance and magnitude limitation
1283 through fault interaction : The case of the 2016 central Italy earthquake sequence.
1284 *Scientific reports*, 9(1), 5005.

1285 Pio Lucente, F., De Gori, P., Margheriti, L., Piccinini, D., Di Bona, M., Chiarabba, C., & Piana
1286 Agostinetti, N. (2010). Temporal variation of seismic velocity and anisotropy before the
1287 2009 MW 6.3 L'Aquila earthquake, Italy. *Geology*, 38(11), 1015-1018.

1288 Pollitz, F. F., Wicks, C. W., Svarc, J. L., Phillips, E., Brooks, B. A., Murray, M. H., & Turner,
1289 R. C. (2022). Postseismic relaxation following the 2019 Ridgecrest, California,
1290 earthquake sequence. *Bulletin of the Seismological Society of America*, 112(2), 734-749.

1291 Proctor, B., Lockner, D., Kilgore, B., Mitchell, T., & Beeler, N. (2020). Direct evidence for
1292 fluid pressure, dilatancy, and compaction affecting slip in isolated faults. *Geophysical*
1293 *Research Letters*, 47(16), e2019GL086767.

1294 Qiu, Q., Barbot, S., Wang, T., & Wei, S. (2020). Slip complementarity and triggering between
1295 the foreshock, mainshock, and afterslip of the 2019 Ridgecrest rupture sequence.
1296 *Bulletin of the Seismological Society of America*, 110(4), 1701-1715.

1297 Reasenber, P. A., & Simpson, R. W. (1992). Response of regional seismicity to the static stress
1298 change produced by the Loma Prieta earthquake. *Science*, 255(5052), 1687-1690.

1299 Rice, J. R. (1992). Chapter 20 Fault Stress States, Pore Pressure Distributions, and the
1300 Weakness of the San Andreas Fault. In *International Geophysics* (Vol. 51, p. 475-503).
1301 Elsevier. [https://doi.org/10.1016/S0074-6142\(08\)62835-1](https://doi.org/10.1016/S0074-6142(08)62835-1)

1302 Rice, J. R., & Cleary, M. P. (1976). Some basic stress diffusion solutions for fluid-saturated
1303 elastic porous media with compressible constituents. *Reviews of Geophysics*, 14(2),
1304 227-241.

1305 Rikitake, T. (1972). Earthquake prediction studies in Japan. *Geophysical surveys*, 1(1), 4-26.

1306 Ripepe, M., Piccinini, D., & Chiaraluce, L. (2000). Foreshock sequence of september 26th,
1307 1997 Umbria-Marche earthquakes. *Journal of Seismology*, 4, 387-399.

1308 Roeloffs, E., Sneed, M., Galloway, D. L., Sorey, M. L., Farrar, C. D., Howle, J. F., & Hughes,
1309 J. (2003). Water-level changes induced by local and distant earthquakes at Long Valley
1310 caldera, California. *Journal of Volcanology and Geothermal Research*, 127(3-4),
1311 269-303.

1312 Ross, Z. E., Trugman, D. T., Hauksson, E., & Shearer, P. M. (2019). Searching for hidden
1313 earthquakes in Southern California. *Science*, 364(6442), 767-771.

- 1314 Ruhl, C., Abercrombie, R., Smith, K., & Zaliapin, I. (2016). Complex spatiotemporal evolution
1315 of the 2008 Mw 4.9 Mogul earthquake swarm (Reno, Nevada) : Interplay of fluid and
1316 faulting. *Journal of Geophysical Research: Solid Earth*, *121*(11), 8196-8216.
- 1317 Sammonds, P., Meredith, P., & Main, I. (1992). Role of pore fluids in the generation of seismic
1318 precursors to shear fracture. *Nature*, *359*(6392), 228-230.
- 1319 Scholz, C. H. (1968). The frequency-magnitude relation of microfracturing in rock and its
1320 relation to earthquakes. *Bulletin of the Seismological Society of America*, *58*(1),
1321 399-415. <https://doi.org/10.1785/BSSA0580010399>
- 1322 Scholz, C. H. (2015). On the stress dependence of the earthquake b value. *Geophysical*
1323 *Research Letters*, *42*(5), 1399-1402.
- 1324 Scholz, C. H. (2019). *The mechanics of earthquakes and faulting*. Cambridge university press.
- 1325 Segall, P. (2010). *Earthquake and volcano deformation*. Princeton University Press.
- 1326 Segall, P., & Rice, J. R. (1995). Dilatancy, compaction, and slip instability of a fluid-infiltrated
1327 fault. *Journal of Geophysical Research: Solid Earth*, *100*(B11), 22155-22171.
- 1328 Serpelloni, E., Anzidei, M., Baldi, P., Casula, G., & Galvani, A. (2005). Crustal velocity and
1329 strain-rate fields in Italy and surrounding regions : New results from the analysis of
1330 permanent and non-permanent GPS networks. *Geophysical Journal International*,
1331 *161*(3), 861-880.
- 1332 Shapiro, S. A. (2015). *Fluid-induced seismicity*. Cambridge University Press.
- 1333 Shi, Y., & Bolt, B. A. (1982). The standard error of the magnitude-frequency b value. *Bulletin*
1334 *of the Seismological Society of America*, *72*(5), 1677-1687.
- 1335 Sibson, R. H. (2000). Fluid involvement in normal faulting. *Journal of Geodynamics*, *29*(3-5),
1336 469-499.
- 1337 Smith, W. D. (1981). The b-value as an earthquake precursor. *Nature*, *289*(5794), 136-139.

- 1338 Soldati, G., Zaccarelli, L., & Faenza, L. (2019). Spatio-temporal seismic velocity variations
1339 associated to the 2016–2017 central Italy seismic sequence from noise cross-correlation.
1340 *Geophysical Journal International*, 219(3), 2165-2173.
- 1341 Stramondo, S., Tesauro, M., Briole, P., Sansosti, E., Salvi, S., Lanari, R., Anzidei, M., Baldi,
1342 P., Fornaro, G., & Avallone, A. (1999). The September 26, 1997 Colfiorito, Italy,
1343 earthquakes : Modeled coseismic surface displacement from SAR interferometry and
1344 GPS. *Geophysical research letters*, 26(7), 883-886.
- 1345 Tan, Y. J., Waldhauser, F., Ellsworth, W. L., Zhang, M., Zhu, W., Michele, M., Chiaraluce, L.,
1346 Beroza, G. C., & Segou, M. (2021). Machine-learning-based high-resolution earthquake
1347 catalog reveals how complex fault structures were activated during the 2016–2017
1348 Central Italy sequence. *The Seismic Record*, 1(1), 11-19.
- 1349 Toda, S., & Stein, R. S. (2020). Long-and short-term stress interaction of the 2019 Ridgecrest
1350 sequence and Coulomb-based earthquake forecasts. *Bulletin of the Seismological*
1351 *Society of America*, 110(4), 1765-1780.
- 1352 Tong, P., Yao, J., Liu, Q., Li, T., Wang, K., Liu, S., Cheng, Y., & Wu, S. (2021). Crustal rotation
1353 and fluids : Factors for the 2019 Ridgecrest earthquake sequence? *Geophysical*
1354 *Research Letters*, 48(3), e2020GL090853.
- 1355 Tormann, T., Wiemer, S., Metzger, S., Michael, A., & Hardebeck, J. L. (2013). Size distribution
1356 of Parkfield’s microearthquakes reflects changes in surface creep rate. *Geophysical*
1357 *Journal International*, 193(3), 1474-1478. <https://doi.org/10.1093/gji/ggt093>
- 1358 Tung, S., & Masterlark, T. (2018). Delayed poroelastic triggering of the 2016 October Visso
1359 earthquake by the August Amatrice earthquake, Italy. *Geophysical Research Letters*,
1360 45(5), 2221-2229.
- 1361 Utsu, T., & Ogata, Y. (1995). The centenary of the Omori formula for a decay law of aftershock
1362 activity. *Journal of Physics of the Earth*, 43(1), 1-33.

- 1363 Wang, K., & Bürgmann, R. (2020). Co- and Early Postseismic Deformation Due to the 2019
1364 Ridgecrest Earthquake Sequence Constrained by Sentinel-1 and COSMO-SkyMed SAR
1365 Data. *Seismological Research Letters*. <https://doi.org/10.1785/0220190299>
- 1366 Wang, K., Dreger, D. S., Tinti, E., Bürgmann, R., & Taira, T. (2020). Rupture process of the
1367 2019 Ridgecrest, California M w 6.4 foreshock and M w 7.1 earthquake constrained by
1368 seismic and geodetic data. *Bulletin of the Seismological Society of America*, 110(4),
1369 1603-1626.
- 1370 Wiemer, S. (2001). A software package to analyze seismicity : ZMAP. *Seismological Research*
1371 *Letters*, 72(3), 373-382.
- 1372 Wiemer, S., & Wyss, M. (2000). Minimum magnitude of completeness in earthquake catalogs :
1373 Examples from Alaska, the western United States, and Japan. *Bulletin of the*
1374 *Seismological Society of America*, 90(4), 859-869.
- 1375 Woessner, J., & Wiemer, S. (2005). Assessing the quality of earthquake catalogues : Estimating
1376 the magnitude of completeness and its uncertainty. *Bulletin of the Seismological Society*
1377 *of America*, 95(2), 684-698.
- 1378 Wyss, M., & Habermann, R. E. (1988). Precursory seismic quiescence. *Pure and Applied*
1379 *Geophysics*, 126(2), 319-332.
- 1380 Wyss, M., & McNutt, S. R. (1998). Temporal and three-dimensional spatial analyses of the
1381 frequency–magnitude distribution near Long Valley Caldera, California. *Geophysical*
1382 *Journal International*, 134(2), 409-421.
- 1383 Wyss, M., & Wiemer, S. (2000). Change in the probability for earthquakes in southern
1384 California due to the Landers magnitude 7.3 earthquake. *Science*, 290(5495),
1385 1334-1338.

- 1386 Xu, X., Sandwell, D. T., & Smith-Konter, B. (2020). Coseismic Displacements and Surface
1387 Fractures from Sentinel-1 InSAR: 2019 Ridgecrest Earthquakes. *Seismological*
1388 *Research Letters*. <https://doi.org/10.1785/0220190275>
- 1389 Yamashita, T., & Tsutsumi, A. (2018a). *Involvement of Fluids in Earthquake Ruptures*.
1390 Springer Japan. <https://doi.org/10.1007/978-4-431-56562-8>
- 1391 Yehya, A., Yang, Z., & Rice, J. R. (2018). Effect of fault architecture and permeability
1392 evolution on response to fluid injection. *Journal of Geophysical Research: Solid Earth*,
1393 *123*(11), 9982-9997.
- 1394 Yue, H., Sun, J., Wang, M., Shen, Z., Li, M., Xue, L., Lu, W., Zhou, Y., Ren, C., & Lay, T.
1395 (2021). The 2019 Ridgecrest, California earthquake sequence : Evolution of seismic and
1396 aseismic slip on an orthogonal fault system. *Earth and Planetary Science Letters*, *570*,
1397 117066.
- 1398